Modular conjugations in 2D conformal field theory and holographic bit threads

Mihail Mintchev[a] **and Erik Tonni**[b]

[a]*Dipartimento di Fisica, Università di Pisa and INFN Sezione di Pisa,*
Largo Bruno Pontecorvo 3, 56127 Pisa, Italy
[b]*SISSA and INFN Sezione di Trieste,*
via Bonomea 265, 34136 Trieste, Italy

E-mail: mintchev@df.unipi.it, erik.tonni@sissa.it

Abstract: We study the geometric action of some modular conjugations in two dimensional (2D) conformal field theories. We investigate the bipartition given by an interval when the system is in the ground state, either on the line or on the circle, and in the thermal Gibbs state on the line. We find that the restriction of the corresponding inversion maps to a spatial slice is obtained also in the gauge/gravity correspondence through the geodesic bit threads in a constant time slice of the dual static asymptotically AdS background. For a conformal field theory in the thermal state on the line, the modular conjugation suggests the occurrence of a second world which can be related through the geodesic bit threads to the horizon of the BTZ black brane background. An inversion map is constructed also for the massless Dirac fermion in the ground state and on the line bipartite by the union of two disjoint intervals.

Contents

1 Introduction

The modular theory of Tomita and Takesaki [1–5], developed within the context of the algebraic quantum field theory, provides important rigorous tools to understand various aspects of the bipartite entanglement in quantum field theories.

Considering a von Neumann algebra $\mathcal{A}$ of observables localised in a spacetime region and in standard form (meaning that it acts on a Hilbert space $\mathcal{H}$ containing a cyclic and separating vector Ω), the conjugate linear operator $S : \mathcal{A}\Omega \to \mathcal{A}\Omega$ is such that $S\,\mathcal{O}\Omega = \mathcal{O}^*\Omega$, for any operator $\mathcal{O} \in \mathcal{A}$. The unique polar decomposition of S reads $S = J\,\Delta^{1/2}$, where Δ is a self adjoint, positive (unbounded in general) operator called modular operator of $(\mathcal{A}, \Omega)$

and J is an antiunitary operator called modular conjugation of $(\mathcal{A}, \Omega)$. It turns out that the vector Ω is invariant, i.e. $\Delta\Omega = \Omega$ and $J\Omega = \Omega$, and also that $J = J^* = J^{-1}$. The modular operator Δ can be written as $\Delta = \mathrm{e}^{-K}$ where K is the (full) modular Hamiltonian, a self adjoint operator whose real spectrum extends in general over $\mathbb{R}$ and such that Ω is one of its eigenvectors with eigenvalue equal to zero. A crucial role is played by the one-parameter group made by the unitary operators $\Delta^{\mathrm{i}\tau}$ with $\tau \in \mathbb{R}$. The theorem of Tomita and Takesaki tells us that $\Delta^{-\mathrm{i}\tau}\mathcal{A}\,\Delta^{\mathrm{i}\tau} = \mathcal{A}$ and $\Delta^{-\mathrm{i}\tau}\mathcal{A}'\,\Delta^{\mathrm{i}\tau} = \mathcal{A}'$ for $\mathcal{A}$ and its commutant $\mathcal{A}'$ for any $\tau \in \mathbb{R}$, and that $J\mathcal{A}J = \mathcal{A}'$. This theorem leads to introduce the group of the modular automorphisms of the state Ω on $\mathcal{A}$, whose generic element is the map $\sigma_\tau \mathcal{O} \equiv \Delta^{\mathrm{i}\tau}\mathcal{O}\,\Delta^{-\mathrm{i}\tau}$, for any $\mathcal{O} \in \mathcal{A}$, which determines the modular evolution (flow) of $\mathcal{O}$ generated by K.

For a local relativistic quantum field theory in its ground state whose space is bipartite by a region A and its complement B in a non trivial way, the theorem of Tomita and Takesaki can be applied and $K = K_A \otimes \mathbf{1}_B - \mathbf{1}_A \otimes K_B$, where K_A and K_B are the modular Hamiltonians of A and B respectively. Typically, σ_τ and J do not have a geometric action; indeed, a direct geometric meaning for σ_τ and J has been found only in very few special cases [2]. The most important one corresponds to the theorem of Bisognano and Wichmann [6, 7], which considers the bipartition associated to half space for a local relativistic quantum field theory in its ground state. In this case the geometric action of σ_τ is given by the Lorentz boosts in the direction preserving the wedge and the geometric action of J by a reflection of the time coordinate and of the spatial coordinate orthogonal to the entangling hyperplane. Another important example is described in the theorem of Hislop and Longo [8, 9], which considers a conformal field theory (CFT) in its ground state and the bipartition determined by a sphere, providing also the geometric actions for the corresponding σ_τ and J. Instead, the action of σ_τ and J is non geometric e.g. for a free massive field theory in its ground state when the space bipartite by a sphere [4, 10, 11].

We consider a local CFT in $1 + 1$ spacetime dimensions (2D). The modular operator Δ in these models has been largely studied and various explicit expressions of modular Hamiltonians have been found, both when the entire system is in its ground state [6–9, 12–22] and in the thermal case [16, 17, 23–32]. Instead, the modular conjugation J and its geometrical action have been less explored [2, 8]. It is worth remarking that the Tomita-Takesaki modular theory provides insightful results when the 2D CFT is in a thermal state, already when the space is the real line. Indeed, the occurrence of a non trivial commutant naturally leads to consider also a *second world* which inherits the structure of the real word through the modular conjugation, as highlighted by Borchers [24], by Schroer and Wiesbrock [25] (who called it virgin spacetime or thermal shadow world) and by Longo et al. [26, 28, 29] (who formalise this idea through the thermal completion).

In this manuscript we study the geometric action of some modular conjugations in 2D CFT by employing the results in the Euclidean spacetime discussed in [17]. They include the case of a 2D CFT in a thermal state on the line bipartite by an interval and the massless Dirac fermion in the ground state on the line bipartite by the union of two disjoint intervals.

In the context of the gauge/gravity (holographic) correspondence, the prescription proposed by Ryu an Takayanagi (RT) [33, 34] to evaluate the holographic entanglement entropy in asymptotically Anti de Sitter (AdS) gravitational backgrounds has provided a

very important tool to explore quantum gravity through quantum information concepts in certain models. Focussing on static gravitational backgrounds, this formula claims that the entanglement entropy S_A of a region A in the dual CFT on the boundary of the asymptotically AdS spacetime can be computed in such dual gravitational background as $S_A = \text{Area}(\gamma_A)/(4G_{\text{N}})$, where G_{N} is the Newton constant and γ_A (often called RT hypersurface) is the codimension-two minimal area hypersurface belonging to the same constant time slice of A, anchored to the boundary of A and homologous to A.

An insightful reformulation of the RT prescription has been suggested by Freedman and Headrick in terms of the holographic bit threads [35]. Consider the bulk vector fields V which are divergenceless $\nabla \cdot V = 0$ and norm bounded as $|V| \leqslant 1$. By applying the Riemannian geometry version of the max-flow/min-cut theorem, it turns out that $\text{Area}(\gamma_A)$ is equal to the maximum flux of one of these vector fields through the spatial region A in the boundary of the asymptotically AdS background. The integral curves (or flow lines) of this vector field are called (holographic) bit threads. In this setting, the RT hypersurface γ_A is the bottleneck of the flow of a vector field satisfying this extremization condition. It is important to remark that, while such vector field is uniquely fixed on γ_A, it is infinitely degenerate on A. Further properties of the holographic bit threads at some fixed time slice have been discussed in [36–40] and also a covariant generalisation has been recently proposed [41]. Some holographic bit threads configurations have been explicitly constructed in [38] by imposing further reasonable requirements in order to reduce the above mentioned degeneracy.

Among the explicit holographic bit threads constructions proposed in [38], in this manuscript we consider the geodesic flows (where the integral lines of the holographic bit threads are also geodesics), showing that, for simple three dimensional gravitational backgrounds and for some bipartitions given by an interval, they provide the same inversion relation obtained from the geometric action of the modular conjugation for the corresponding setup in the dual CFT.

The outline of the paper is as follows. In section 2 the main quantities considered throughout our analyses are introduced. The CFT analysis for the simplest case, which involves the bipartition of the line given by a single interval when the entire system is in the ground state, is carried out in section 3. In section 4 the results of the previous section are related to the geodesic bit threads in a constant time slice of Poincaré AdS$_3$. In section 5 we discuss the geometric action of the modular conjugation for a CFT in a thermal state and on the line bipartite by an interval. In section 6, the resulting inversion map is related to the geodesic bit threads in the BTZ black brane geometry. In section 7 we propose an inversion map for the free massless Dirac field in the ground state and on the line bipartite by the union of two disjoint intervals. Some conclusions are drawn in section 8. In appendix A we explore the inversion map for a CFT on a circle bipartite by an interval and in its ground state, and in appendix B we discuss the corresponding holographic construction through geodesic bit threads in a constant time slice of global AdS$_3$.

2 Single interval: modular flow of a chiral field

In this section we summarise some basic results about the modular Hamiltonians in 2D CFT and their modular flows employed in the rest of the paper [8, 9, 12, 15–17, 21, 30].

In the $1+1$ dimensional Minkowski spacetime $\mathcal{M}$ described by the coordinates (x, t), we consider the light ray coordinates

$$u_\pm \equiv x \pm t \tag{2.1}$$

and a right $(+)$ and a left $(-)$ primary chiral field $\phi_\pm(u_\pm)$ of dimension h. Such fields satisfy the following commutation relation [42]

$$\left[\, T_\pm(u_\pm) \,,\, \phi_\pm(v_\pm) \,\right] \,=\, \mathrm{i}\left(\delta(u_\pm - v_\pm)\,(\partial\phi_\pm)(v_\pm) - h\,\phi_\pm(v_+)\,\delta'(u_\pm - v_\pm) \right) \tag{2.2}$$

where $T_\pm$ are the chiral components of the energy-momentum tensor. For the cases we are interested in, the right and left modular Hamiltonians of a single interval $A = [a, b]$ can be written in terms of $T_\pm$ as follows

$$K_A^\pm \,=\, \pm\, 2\pi \int_a^b \beta_0(u_\pm)\, T_\pm(u_\pm)\, \mathrm{d}u_\pm \tag{2.3}$$

with

$$\beta_0(u) \equiv \frac{1}{w'(u)} \tag{2.4}$$

where the explicit form of the function w depends on the state of the entire system. For instance, in the ground state we have

$$w(u) = \log\left(\frac{u - a}{b - u}\right) \qquad \beta_0(u) \equiv \frac{(b - u)(u - a)}{b - a}\,. \tag{2.5}$$

At finite temperature $1/\beta$, we consider a thermal state for which the mean energy density satisfies the Stefan-Boltzmann law [43]

$$\langle T_{tt}(t, x) \rangle \equiv \frac{1}{2}\, \langle T_+(x + t) + T_-(x - t) \rangle \,=\, \frac{c\,\pi}{12\,\beta^2} \tag{2.6}$$

where c is the central charge of the 2D CFT. According to [28, 29], for $0 < c < 1$ this state is unique, while for $c \geqslant 1$ the condition (2.6) selects a specific (geometric) thermal state. In this case

$$w(u) = \log\left(\frac{\sinh[\pi(u - a)/\beta]}{\sinh[\pi(b - u)/\beta]}\right) \qquad \beta_0(u) \equiv \frac{\beta}{\pi}\, \frac{\sinh[\pi(b - u)/\beta]\,\sinh[\pi(u - a)/\beta]}{\sinh[\pi(b - a)/\beta]}\,. \tag{2.7}$$

The modular evolution (flow) of $\phi_\pm$, generated by (2.3), reads

$$\phi_\pm(\tau, u_\pm) \equiv \mathrm{e}^{\mathrm{i}\tau K_A^\pm}\, \phi_\pm(u_\pm)\, \mathrm{e}^{-\mathrm{i}\tau K_A^\pm} \tag{2.8}$$

$$= \left[\frac{\beta_0\big(\xi(\pm\tau, u_\pm)\big)}{\beta_0(u_\pm)} \right]^h \phi_\pm\big(\xi(\pm\tau, u_\pm)\big) = \left[\partial_{u_\pm}\xi(\pm\tau, u_\pm)\right]^h \phi_\pm\big(\xi(\pm\tau, u_\pm)\big)$$

(see e.g. the appendix B of [21]), where $\tau \in \mathbb{R}$ is the modular parameter and the function $\xi(\tau, u)$ is fully determined by the function w as follows

$$\xi(\tau, u) = w^{-1}\big(w(u) + 2\pi\,\tau\big) \tag{2.9}$$

– 4 –

where $u \in A$. Since $\xi(0, u) = u$ for any $u \in A$ by construction, the fields in (2.8) satisfy the initial condition $\phi_\pm(0, u_\pm) = \phi_\pm(u_\pm)$.

In our analyses we also employ the modular evolution in Euclidean spacetimes described in [17], which is given by a complex function related to (2.9) as follows

$$z(\theta, x) = \xi\left(\frac{\mathrm{i}\theta}{2\pi}, x\right) = w^{-1}(w(x) + \mathrm{i}\theta) \tag{2.10}$$

where $x \in A$ and $\theta \in [0, 2\pi)$.

A fundamental characteristic feature of any modular flow is the Kubo-Martin-Schwinger (KMS) condition [2]. In order to check that the flow (2.8) satisfies this condition, consider the two-point functions

$$W_\pm(\tau_1, t_1, x_1; \tau_2, t_2, x_2) \equiv \langle \phi_\pm(\tau_1, x_1 \pm t_1)\, \phi_\pm(\tau_2, x_2 \pm t_2) \rangle \tag{2.11}$$

where x_1 and x_2 belong to A. The KMS condition implies

$$W_\pm(\tau_1 + \mathrm{i}, t_1, x_1\,; \tau_2, t_2, x_2) \,=\, W_\pm(\tau_1, t_1, x_1; \tau_2 + \mathrm{i}, t_2, x_2, t_2) \,=\, W_\pm(\tau_2, t_2, x_2; \tau_1, t_1, x_1) \tag{2.12}$$

which can be verified deriving the expectation values (2.11) in explicit form. To deal with the left and right movers simultaneously, let us adopt the notation

$$\phi(u) = \begin{cases} \phi_+(u) & u = u_+ \\ \phi_-(u) & u = u_- \,. \end{cases} \tag{2.13}$$

From (2.8), for the two-point function along the modular flow one obtains

$$\langle \phi(\tau_1, u_1)\, \phi(\tau_2, u_2) \rangle = \left[\partial_{u_1} \xi(\tau_1, u_1)\, \partial_{u_2} \xi(\tau_2, u_2) \right]^h \langle \phi(\xi(\tau_1, u_1))\, \phi(\xi(\tau_2, u_2)) \rangle \tag{2.14}$$

where the expectation value in the r.h.s. is determined by the choice of representation for ϕ. In the ground state and in the thermal state, we have respectively

$$\langle \phi(u_1)\, \phi(u_2) \rangle = \frac{1}{2\pi\mathrm{i}\,(u_1 - u_2 - \mathrm{i}\varepsilon)^{2h}} \qquad \langle \phi(u_1)\, \phi(u_2) \rangle = \frac{1}{2\pi\mathrm{i}\left[\frac{\beta}{\pi}\,\sinh\left(\frac{\pi}{\beta}(u_1 - u_2 - \mathrm{i}\varepsilon)\right)\right]^{2h}}\,. \tag{2.15}$$

Combining these expressions with (2.8), in the ground state one finds

$$\langle \phi(\tau_1, u_1)\, \phi(\tau_2, u_2) \rangle = \frac{1}{2\pi\mathrm{i}} \left[\frac{1}{u_1 - u_2 - \mathrm{i}\varepsilon}\, \frac{e^{w(u_1)} - e^{w(u_2)}}{e^{w(u_1) + \pi\tau_{12}} - e^{w(u_2) - \pi\tau_{12}} - \mathrm{i}\varepsilon} \right]^{2h} \tag{2.16}$$

with $\tau_{12} \equiv \tau_1 - \tau_2$ and w given by (2.5). Instead, at finite temperature one has

$$\langle \phi(\tau_1, u_1)\, \phi(\tau_2, u_2) \rangle = \frac{1}{2\pi\mathrm{i}} \left[\frac{1}{\frac{\beta}{\pi}\,\sinh\left(\frac{\pi}{\beta}(u_1 - u_2 - \mathrm{i}\varepsilon)\right)}\, \frac{e^{w(u_1)} - e^{w(u_2)}}{e^{w(u_1) + \pi\tau_{12}} - e^{w(u_2) - \pi\tau_{12}} - \mathrm{i}\varepsilon} \right]^{2h} \tag{2.17}$$

with w defined by (2.7). By using the explicit expressions (2.16) and (2.17), one can directly verify the KMS condition (2.12).

We observe also that, in addition to (2.12), the thermal two-point function (2.17) satisfies the KMS condition in the physical time

$$W_\pm(\tau_1, t_1 + \mathrm{i}\beta, x_1; \tau_2, t_2, x_2) = W_\pm(\tau_1, t_1, x_1; \tau_2, t_2 + \mathrm{i}\beta, x_2) = W_\pm(\tau_2, t_2, x_2; \tau_1, t_1, x_1) \tag{2.18}$$

which involves β.

In the $1+1$ dimensional Minkowski spacetime in the coordinates (x, t), let us consider the domain of dependence $\mathcal{D}_A$ of the interval $A = [a, b] \in \mathbb{R}$ (also known as diamond or double cone). A modular trajectory in $\mathcal{D}_A$ is made by the points whose spacetime coordinates are

$$x(\tau) = \frac{\xi(\tau, u_{+,0}) + \xi(-\tau, u_{-,0})}{2} \qquad\qquad t(\tau) = \frac{\xi(\tau, u_{+,0}) - \xi(-\tau, u_{-,0})}{2} \tag{2.19}$$

in terms of (2.9), where $\tau \in \mathbb{R}$ and $u_{\pm,0}$ are the light ray coordinates of the point at $\tau = 0$. It is often convenient to describe a modular trajectory in terms of the point $x \in A$ at $t = 0$. Setting $\tau = 0$ at this point, this modular trajectory is given by $(x(\tau), t(\tau)) \in \mathcal{D}_A$ with

$$x(\tau) = \frac{\xi(\tau, x) + \xi(-\tau, x)}{2} \qquad\qquad t(\tau) = \frac{\xi(\tau, x) - \xi(-\tau, x)}{2} \tag{2.20}$$

in terms of (2.9), where $\tau \in \mathbb{R}$.

3 Single interval: ground state

In this section we focus on a CFT in the ground state and on the line bipartite by an interval $A = (a, b) \subset \mathbb{R}$ and its complement.

3.1 Internal modular evolution

The function w to consider in this case is given in (2.5) [8, 12, 15–17]. Specifying (2.9) to this function, for each chirality we obtain the following geometric action of the modular operator [2, 8, 9][1]

$$\xi(\tau, u) = \frac{a + b\, \mathrm{e}^{w(u)}\, \mathrm{e}^{2\pi\tau}}{1 + \mathrm{e}^{w(u)}\, \mathrm{e}^{2\pi\tau}} = \frac{(b-u)\, a + (u-a)\, b\, \mathrm{e}^{2\pi\tau}}{b - u + (u-a)\, \mathrm{e}^{2\pi\tau}} \qquad\qquad \xi(\tau = 0, u) = u \tag{3.1}$$

which is also known as the geometric action of the modular automorphism group of the diamond $\mathcal{D}_A$ induced by the vacuum state. The expression (3.1) must be employed for both the chiralities and it provides the modular trajectories in the diamond $\mathcal{D}_A$ through (2.19), or (2.20) equivalently.

For any assigned $x \in (a, b)$, from (3.1) we have that the functions in (2.20) satisfy $x(\tau = 0) = x$ and $t(\tau = 0) = 0$, as expected. Notice that $\xi(\pm\tau, x)$ take all real values for $\tau \in \mathbb{R}$, with $\xi(\tau, x) \to a$ as $\tau \to -\infty$ and $\xi(\tau, x) \to b$ as $\tau \to +\infty$. Moreover, $\xi(\tau, a) = a$ and $\xi(\tau, b) = b$ for any $\tau \in \mathbb{R}$. In the left panel of figure 1, the solid curves in the grey region correspond to $\xi(\tau, x)$ and $\xi(-\tau, x)$, with $\tau \in \mathbb{R}$. These curves intersect at $x \in (a, b)$, when $\tau = 0$.

---

[1]The eq. (V.4.33) of [2] is obtained by setting $b = -a = 1$ and $\tau_{\mathrm{here}} = -\tau_{\mathrm{there}}$ in (3.1).
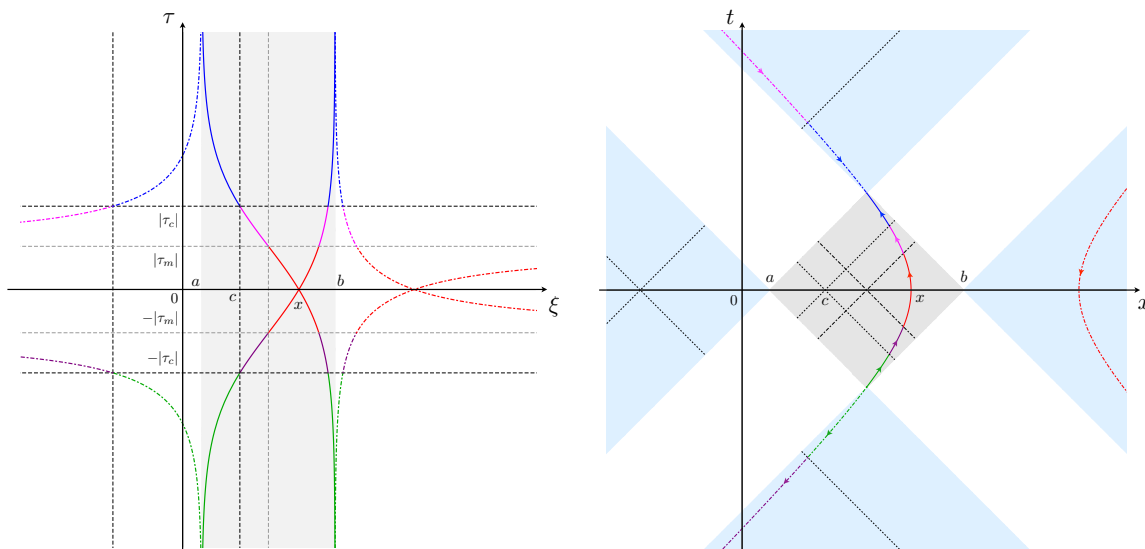
Figure 1. Left: the curves for $\xi(\tau, x)$ and $\xi(-\tau, x)$ (solid lines) and for $\xi(\tau, z_{\text{inv}}(x))$ and $\xi(-\tau, z_{\text{inv}}(x))$ (dot-dashed lines), obtained from (3.1), (3.8) and (3.4). Right: modular trajectory (solid line) in the diamond $\mathcal{D}_A$ (grey region) and its image under the inversion (3.3) (dot-dashed line) in $\mathcal{W}_A$. The dot-dashed segment in $\mathcal{D}_A$ provide the partition (3.2). The modular parameter τ grows along the curves as indicated by the arrows. The modular trajectory and its inversion provide the hyperbola (3.10).

Given a generic $c \in (a, b)$, from (2.9) we have that $\xi(\tau_c, x) = c$ when $\tau_c = \frac{1}{2\pi}[w(c) - w(x)]$. This value splits the range of the modular parameter $\tau \in \mathbb{R}$ into three sets $(-\infty, -|\tau_c|)$, $(-|\tau_c|, |\tau_c|)$ and $(|\tau_c|, +\infty)$, as highlighted by the darker grey horizontal dashed lines in the left panel of figure 1. A special role is played by the mid-point of the interval $\frac{a+b}{2}$ (see section 3.2)), which corresponds to the value $\tau_m = \frac{1}{2\pi}[w(\frac{a+b}{2}) - w(x)]$ of the modular parameter, that provides the lighter grey horizontal lines in the left panel of figure 1.

The important case considered by Bisognano and Wichmann [6, 7] corresponds to the limiting regime where the subsystem A becomes the semi-infinite line $x > 0$. Setting $a = 0$ first and then taking $b \to +\infty$ in (3.1), one finds $\xi(\tau, x) = x\, e^{2\pi\tau}$ with $x > 0$, i.e. the dilations of the semi-infinite line parameterised by τ.

The action of the modular operator and of the modular conjugation in the Minkowski space can be found by combining the corresponding actions for the two chiralities. In the right panel of figure 1, the grey region is the domain of dependence $\mathcal{D}_A$ of the interval $A = [a, b] \in \mathbb{R}$, which is also called diamond or double cone. The null rays departing from its central point $(\frac{a+b}{2}, 0)$ (dot-dashed segments in $\mathcal{D}_A$) provide the following partition of $\mathcal{D}_A$ into four smaller diamonds

$$\mathcal{D}_A \equiv \mathcal{D}_{\text{R}} \cup \mathcal{D}_{\text{L}} \cup \mathcal{D}_{\text{F}} \cup \mathcal{D}_{\text{P}} \tag{3.2}$$

where in the r.h.s. the letter in the subindex stands for either right (R) or left (L) or future (F) or past (P), depending on the position of the corresponding diamond with respect to

the central point $(\frac{a+b}{2}, 0)$ of $\mathcal{D}_A$. The latter point is the only one which provides a partition of $\mathcal{D}_A$ in four diamonds; indeed, the partitions of $\mathcal{D}_A$ induced by the other points include at least two rectangular regions. The solid line inside $\mathcal{D}_A$ is the modular trajectory obtained from (2.20), with $\xi(\tau, x)$ and $\xi(-\tau, x)$ given by the solid lines shown in left panel of the same figure (an arc having certain colour in the left panel provides the arc with the same colour in the right panel). The different arcs of the modular trajectory in $\mathcal{D}_A$ can be identified through their intersections with the light rays departing from $(c, 0)$ (dotted segments in $\mathcal{D}_A$) and from the mid-point of the interval at $t = 0$ (dot-dashed segments in $\mathcal{D}_A$). The modular parameter τ grows along the modular trajectory as indicated by the arrows.

When A becomes the semi-infinite line $x > 0$ (i.e. for $a = 0$ and $b \to +\infty$), the modular trajectory obtained from (3.1) and (2.20) simplifies to $(x(\tau), t(\tau)) = (x \cosh(\tau), x \sinh(\tau))$.

3.2 Geometric action in Minkowski spacetime

For a CFT in the ground state and on the line bipartite through an interval, the geometric action of the modular conjugation is the following inversion map $(x, t) \to (x_{\rm inv}, t_{\rm inv})$ [2, 8][2]

$$x_{\rm inv}(x, t) \equiv \frac{a+b}{2} - \left(\frac{b-a}{2}\right)^2 \frac{x - \frac{a+b}{2}}{t^2 - \left(x - \frac{a+b}{2}\right)^2} \qquad t_{\rm inv}(x, t) \equiv \left(\frac{b-a}{2}\right)^2 \frac{t}{t^2 - \left(x - \frac{a+b}{2}\right)^2} \tag{3.3}$$

which is idempotent, as expected.

In terms of the light ray coordinates (2.1), the geometric action (3.3) leads to define the inversion map $z_{\rm inv}$ as follows

$$u_{\pm, \rm inv}(u_\pm) \equiv x_{\rm inv}(x, t) \pm t_{\rm inv}(x, t) = \frac{a+b}{2} + \frac{(\frac{b-a}{2})^2}{u_\pm - \frac{a+b}{2}} \equiv z_{\rm inv}(u_\pm) \tag{3.4}$$

which allows to write (3.3) as

$$x_{\rm inv}(x, t) = \frac{z_{\rm inv}(x+t) + z_{\rm inv}(x-t)}{2} \qquad t_{\rm inv}(x, t) = \frac{z_{\rm inv}(x+t) - z_{\rm inv}(x-t)}{2}. \tag{3.5}$$

Another insightful form of the geometric action of the modular conjugation can be written in terms of the distance from the mid-point of A. Indeed, by introducing

$$\tilde{x} \equiv x - \frac{a+b}{2} \qquad \tilde{x}_{\rm inv} \equiv x_{\rm inv} - \frac{a+b}{2} \tag{3.6}$$

from (3.3) one finds that

$$\tilde{x}_{\rm inv} \pm t_{\rm inv} = \frac{(\ell/2)^2}{\tilde{x} \pm t} \tag{3.7}$$

where $\ell \equiv b - a$ is the length of the interval A, whose endpoints are the entangling points.

When $t = 0$, the inversion map (3.3) simplifies to

$$x_{\rm inv}(x, t = 0) = z_{\rm inv}(x) \qquad t_{\rm inv}(x, t = 0) = 0 \tag{3.8}$$

which sends A into its complement on the line, and viceversa. In particular, $z_{\rm inv}(x) < a$ when $x \in (a, \frac{a+b}{2})$ and $z_{\rm inv}(x) > b$ when $x \in (\frac{a+b}{2}, b)$. We remark that $z_{\rm inv}(x)$ in (3.8) sends

---

[2]The two dimensional case of eq. (V.4.34) in [2] corresponds to (3.3) for $b = -a = 1$.

a point in A close to an entangling point into a point in B close to the same entangling point, and viceversa.

In the left panel of figure 1 the dot-dashed curves correspond to $\xi(\tau, z_{\mathrm{inv}}(x))$ and $\xi(-\tau, z_{\mathrm{inv}}(x))$, with $\tau \in \mathbb{R}$, which intersect at $\tau = 0$ and $z_{\mathrm{inv}}(x) \in B$. These curves and the corresponding ones for $\xi(\tau, x)$ and $\xi(-\tau, x)$ in the grey region are partitioned into five arcs (indicated with different colours) at the values $\tau = \mp|\tau_c|$ and $\tau = \mp|\tau_m|$ of the modular parameter. Notice that, while $|\xi(\tau, x)|$ remains finite, we have that $|\xi(\tau, z_{\mathrm{inv}}(x))| \to +\infty$ as $|\tau| \to |\tau_m|$; hence, in the left panel of figure 1 the value τ_m provides the asymptotes $\tau = \pm|\tau_m|$ (lighter grey horizontal lines) for the red dot-dashed lines.

In the right panel of figure 1, the light blue region $\mathcal{W}_A$ can be partitioned into four infinite triangular domains as follows

$$\mathcal{W}_A \equiv \mathcal{W}_{\mathrm{R}} \cup \mathcal{W}_{\mathrm{L}} \cup \mathcal{V}_{\mathrm{F}} \cup \mathcal{V}_{\mathrm{P}} \tag{3.9}$$

(the notation introduced in (3.2) has been adopted also here) where the subindex indicates the position of the vertex of the corresponding infinite triangle with respect to the center of $\mathcal{D}_A$. The vertices of the left spacelike wedge $\mathcal{W}_{\mathrm{L}}$ and the right spacelike wedge $\mathcal{W}_{\mathrm{R}}$ are $(a, 0)$ and $(b, 0)$ respectively, while the forward light cone $\mathcal{V}_{\mathrm{F}}$ and backward light cone $\mathcal{V}_{\mathrm{P}}$ have vertices in $(\frac{a+b}{2}, \frac{b-a}{2})$ and $(\frac{a+b}{2}, -\frac{b-a}{2})$ respectively. The geometric action of the modular conjugation given by (3.3), or equivalently by (3.4) in the light ray coordinates, maps $\mathcal{D}_A$ into the light blue region and viceversa (see also figure V.4.1 of [2]). The mid-point $(\frac{a+b}{2}, 0)$ is sent to infinity by this map. Considering the geometric action (3.3) separately on each element of the partitions of $\mathcal{D}_A$ and $\mathcal{W}_A$ introduced in (3.2) and (3.9), one finds that it relates domains that share a vertex (hence with the same subindex).

The modular trajectory $\{(x(\tau), t(\tau)); \tau \in \mathbb{R}\}$ corresponding to the solid curve in $\mathcal{D}_A$, which passes through $(x, 0)$ when $\tau = 0$ and has been obtained from (3.1) and (2.20), is mapped through the inversion (3.3) into the dot-dashed curve $\{(\tilde{x}(\tau), \tilde{t}(\tau)); \tau \in \mathbb{R}\}$ in $\mathcal{W}_A$. The latter trajectory can be also constructed by combining (3.1), (2.20) and (3.8) and passes through $(z_{\mathrm{inv}}(x), 0)$ when $\tau = 0$. The modular parameter τ grows along these curves as indicated by the arrows. Hence, both the modular trajectory in $\mathcal{D}_A$ and its dot-dashed image in $\mathcal{W}_A$ originate in the lower vertex of $\mathcal{D}_A$ as $\tau \to -\infty$ and end in the upper vertex of $\mathcal{D}_A$ as $\tau \to +\infty$. Each arc in the modular trajectory having a certain colour is sent by (3.3) to the arc on the dot-dashed curve having the same colour and they both correspond to the same range of the modular parameter τ. As already remarked, the partition of the modular trajectory into the five arcs with different colours is determined by its intersections with the light rays departing from the mid-point of the interval $P_m = (\frac{a+b}{2}, 0)$ (black dot-dashed segments in $\mathcal{D}_A$) and from the generic point $P_c = (c, 0)$ in the interval (black dotted segments in $\mathcal{D}_A$) at $t = 0$. The same holds for the image of the modular trajectory under (3.3) in the light blue region, with the obvious difference that its partition is determined by the light rays departing from the images of P_m and P_c under the same map. Since this map sends P_m to infinity, the red, purple and magenta dot-dashed arcs in the light blue region reach infinity in $\mathcal{W}_{\mathrm{R}}$, $\mathcal{V}_{\mathrm{P}}$ and $\mathcal{V}_{\mathrm{F}}$ respectively. In particular, the red dot-dashed arc in $\mathcal{W}_A$ entirely belongs either to $\mathcal{W}_{\mathrm{R}}$ or to $\mathcal{W}_{\mathrm{L}}$, depending on whether $x > \frac{a+b}{2}$ or $x < \frac{a+b}{2}$ respectively, and (3.8) tells us that it

passes through the point $(z_{\text{inv}}(x), 0)$ when $\tau = 0$. Any arc in the right panel of figure 1 is obtained through (2.20), by using the arcs denoted by the same kind of line and the same colour in the left panel of the same figure.

Merging all the solid and the dot-dashed arcs in the right panel of figure 1, for $x \neq \frac{a+b}{2}$ one obtains the hyperbola given by[3]

$$\left[x(\tau) - x_0\right]^2 - t(\tau)^2 = \kappa^2 \qquad\qquad \left[\tilde{x}(\tau) - x_0\right]^2 - \tilde{t}(\tau)^2 = \kappa^2 \qquad\qquad (3.10)$$

in $\mathcal{D}_A$ and $\mathcal{W}_A$ respectively, with

$$x_0 \equiv \frac{x^2 - a\,b}{2(x - \frac{a+b}{2})} \qquad\qquad \kappa \equiv \frac{(b-x)\,(x-a)}{2(x - \frac{a+b}{2})}\,. \qquad\qquad (3.11)$$

The semi-axes of the hyperbola (3.10) are both equal to κ and its center is $(x_0, 0)$, where $x_0 = \frac{1}{2}[x + z_{\text{inv}}(x)]$; hence its asymptotes have slopes equal to ± 1 and pass through $(x_0, 0)$. Since $x_0 - b = (b-x)^2/[2(x - \frac{a+b}{2})]$ when $x \in (\frac{a+b}{2}, b)$ and $a - x_0 = (a-x)^2/[2(\frac{a+b}{2} - x)]$ when $x \in (a, \frac{a+b}{2})$ are both positive, the center of the hyperbola (3.10) belongs to $\mathcal{W}_A$ for any initial value $x \in A$ different from the middle point $\frac{a+b}{2}$.

It is worth considering two special bipartitions of the line. When $a = -b$, the interval A is centered in the origin of the x-axis and the inversion map (3.3) becomes [2][4]

$$x_{\text{inv}} = -\frac{b^2\,x}{t^2 - x^2} \qquad\qquad t_{\text{inv}} = \frac{b^2\,t}{t^2 - x^2} \qquad\qquad (3.12)$$

which further simplifies for $t = 0$ to the following suggestive form

$$x_{\text{inv}} = \frac{b^2}{x} \qquad\qquad t_{\text{inv}} = 0\,. \qquad\qquad (3.13)$$

When $b \to +\infty$, the interval A and its diamond $\mathcal{D}_A$ become respectively the half line $x \geqslant a$ and the right Rindler wedge with vertex in $(a, 0)$. The inversion map (3.3) simplifies to the modular conjugation for such Rindler wedge, which reads [2][5]

$$x_{\text{inv}}(x, t) - a = -(x - a) \qquad\qquad t_{\text{inv}}(x, t) = -t\,. \qquad\qquad (3.14)$$

In terms of the light ray coordinates (2.1), taking $b \to +\infty$ in (3.4), for this map one obtains

$$u_{\pm,\text{inv}} - a = -(u_\pm - a) \qquad\qquad (3.15)$$

which is consistent with (3.14), as expected.

The above results can be extended in a straightforward way to the case in higher dimensions where the subsystem is a spatial sphere in the Minkowski spacetime [2, 8], by employing the light cone coordinates $r \pm t$, being r the radial coordinate when the origin coincides with the center of the sphere.

---

[3]We are grateful to an anonymous referee for a comment that led us to this observation.

[4]The eq. (V.4.34) of [2] corresponds to (3.12) for $b = 1$.

[5]The case $a = 0$ of (3.14) is discussed in section V.4.2 of [2].

3.3 Geometric action in the Euclidean spacetime

In [17] the modular evolution in the Euclidean spacetime for a 2D CFT in its ground state and on a line bipartite by an interval $A = (a, b)$ has been described in terms of the function $w(x)$ given in (2.5) through the following complex function

$$z(\theta, x) \equiv w^{-1}(w(x) + \mathrm{i}\theta) = \frac{a\,(b-x) + b\,(x-a)\,\mathrm{e}^{\mathrm{i}\theta}}{b - x + (x-a)\,\mathrm{e}^{\mathrm{i}\theta}} \qquad \theta \in [0, 2\pi) \qquad x \in A \quad (3.16)$$

which can be obtained also by replacing $2\pi\tau$ with $\mathrm{i}\theta$ in (3.1). This complex function can be equivalently written in the form

$$z(\theta, x) = \mathcal{C} + \mathcal{R}\,\mathrm{e}^{\mathrm{i}\gamma} \tag{3.17}$$

where

$$\mathcal{C} \equiv \frac{x^2 - a\,b}{2\big(x - \frac{a+b}{2}\big)} \qquad \mathcal{R} \equiv \frac{(b-x)(x-a)}{2\big(x - \frac{a+b}{2}\big)} \qquad \gamma \equiv \pi - \theta - \mathrm{i}\log\!\left(\frac{x - a + \mathrm{e}^{\mathrm{i}\theta}(b-x)}{x - a + \mathrm{e}^{-\mathrm{i}\theta}(b-x)}\right). \tag{3.18}$$

Hence, in the complex plane described by the complex coordinate z, the curve $z(\theta, x)$ corresponding to an assigned value $x \in A$ and parameterised by $\theta \in (0, 2\pi)$ is a circle with radius $\mathcal{R}$ centered in the point $(\mathcal{C}, 0)$ on the real axis. From (3.16), notice that $z(\theta, a) = a$ and $z(\theta, b) = b$ for any allowed value of θ, despite the fact that $w(x)$ in (2.5) is not defined when either $x = a$ or $x = b$.

In figure 2, considering the complex plane described by the complex variable z (grey plane), we show the half circles obtained from (3.16) (or (3.17) equivalently) for various assigned $x \in A$ and parameterised either by $\theta \in (0, \pi)$ (solid arcs) or by $\theta \in (\pi, 2\pi)$ (dot-dashed arcs). In the same complex plane, it is useful to explore also the curves given by (3.16) (or (3.17) equivalently) parameterised by $x \in A$ for some fixed $\theta \in (0, 2\pi)$. For these curves we have that $\partial_x z(\theta, x) \to \mathrm{e}^{\mathrm{i}\theta}$ as $x \to a$ and $\partial_x z(\theta, x) \to \mathrm{e}^{-\mathrm{i}\theta}$ as $x \to b$; hence, the curve that intersects orthogonally the real axis at $x = a$ and $x = b$ corresponds to $\theta = \pi/2$. From (3.16) one finds that such curve is the half circle centered in the mid-point of A (see also section 4 and figure 3).

The inversion map (3.4) naturally provides the complex map $z_{\mathrm{inv}} : \mathbb{C} \to \mathbb{C}$ given by

$$z_{\mathrm{inv}}(\zeta) = \frac{a+b}{2} + \frac{\big(\frac{b-a}{2}\big)^2}{\zeta - \frac{a+b}{2}} \tag{3.19}$$

which is a rational function with real parameters. By introducing the real variable $t_{\mathrm{E}} \in \mathbb{R}$ and exploiting (3.5), we can relate (3.19) to the inversion map (3.3) by replacing t with $\mathrm{i}t_{\mathrm{E}}$, finding

$$\mathrm{Re}\big[z_{\mathrm{inv}}(x + \mathrm{i}t_{\mathrm{E}})\big] = \frac{z_{\mathrm{inv}}(x + \mathrm{i}t_{\mathrm{E}}) + z_{\mathrm{inv}}(x - \mathrm{i}t_{\mathrm{E}})}{2} = x_{\mathrm{inv}}(x, \mathrm{i}t_{\mathrm{E}}) \tag{3.20}$$

$$\mathrm{i}\,\mathrm{Im}\big[z_{\mathrm{inv}}(x + \mathrm{i}t_{\mathrm{E}})\big] = \frac{z_{\mathrm{inv}}(x + \mathrm{i}t_{\mathrm{E}}) - z_{\mathrm{inv}}(x - \mathrm{i}t_{\mathrm{E}})}{2} = t_{\mathrm{inv}}(x, \mathrm{i}t_{\mathrm{E}}). \tag{3.21}$$
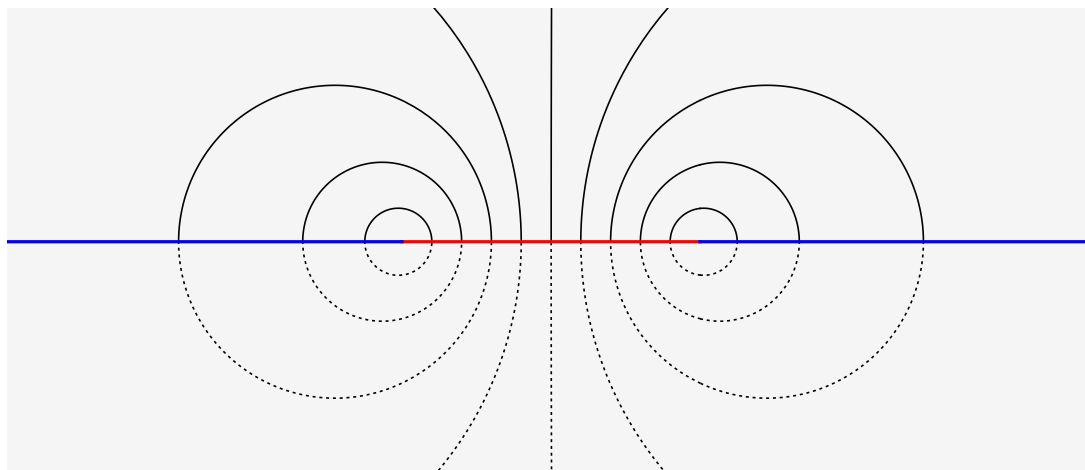
Figure 2. Euclidean modular evolution in the complex plane: the curves are half circles obtained from (3.16) (or (3.17) equivalently) with $\theta \in (0, \pi)$ (solid arcs) or $\theta \in (\pi, 2\pi)$ (dotted arcs), for some $x \in A$. They map a point in A (red segment) to a point in its complement (blue half lines) and viceversa, which are related by (3.22).

The inversion on the real line given in (3.8) can be obtained by restricting (3.19) to the real line or by evaluating (3.16) at $\theta = \pi$, which is equivalent to (2.9) evaluated at $\tau = \mathrm{i}/2$, namely

$$z_{\mathrm{inv}}(x) = z(\pi, x) = \xi(\mathrm{i}/2, x) \qquad x \in \mathbb{R}\,. \tag{3.22}$$

This tells us that, in figure 2, the endpoints of a black solid half circle in the upper half plane (or of the corresponding black dotted half circle in the lower half plane) belong to the real axis and are related through the inversion map (3.8). Hence, any point in the interval A (red segment) is uniquely mapped into a point in its complement on the line (union of the blue half lines), and viceversa. From (3.22), we also observe that (3.16) e (3.19) are related as follows

$$z_{\mathrm{inv}}(\zeta) = z(\pi, \zeta) \qquad \zeta \in \mathbb{C}\,. \tag{3.23}$$

Finally, by combining (3.22) with (3.5) and (3.16) (or (2.9)), one observes that the geometric action of the modular conjugation (3.3) can be expressed through $w(x)$ in (2.5).

4 Geodesic bit threads in Poincaré AdS₃

In this section we relate the geodesic bit threads in Poincaré AdS₃ for the RT curve corresponding to an interval on the line to the results discussed in section 3.2 and section 3.3.

The Poincaré AdS₃ can be described by the coordinates (t, x, ζ), where $\zeta > 0$ parameterises the holographic direction, hence its boundary corresponds to $\zeta = 0$. A $t = \text{const}$ slice of Poincaré AdS₃ is the upper half plane described by the coordinates (x, ζ) and equipped with the following metric (yellow region in figure 3)

$$ds^2 = \frac{dx^2 + d\zeta^2}{\zeta^2} \qquad \zeta > 0\,. \tag{4.1}$$
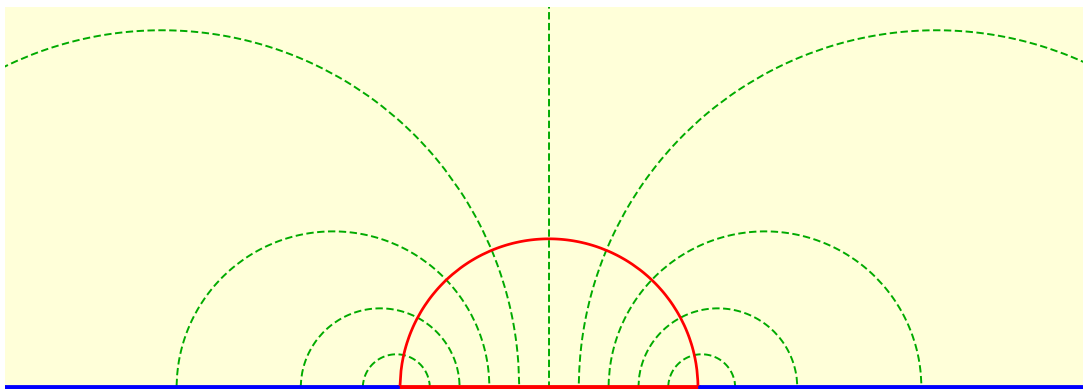
Figure 3. Geodesic bit threads (green dashed curves) in a fixed time slice of Poincaré AdS$_3$ (yellow region) associated to an interval on the line (red segment), whose RT curve is the red solid half circle anchored to its endpoints.

In this Euclidean manifold, the set of geodesics having both the endpoints on the boundary is the two-parameter family of half circles centered on the x-axis, namely

$$(x - x_s)^2 + \zeta^2 = R_s^2 \,. \tag{4.2}$$

The vertical lines orthogonal to the boundary provide the remaining set of geodesics. According to the AdS/CFT correspondence, on the boundary of the Poincaré AdS$_3$ we have a dual 2D CFT on the real line and in its ground state.

In order to recover the same situation investigated in section 3, the spatial direction on the boundary is bipartite by an interval of length $\ell \equiv 2b$ (red segment in figure 3) and its complement (union of the blue half lines in figure 3). The interval can be placed symmetrically with respect to the origin (i.e. $A = \{x \,; |x| \leqslant b\}$) without loss of generality. The RT formula [33, 34] provides the holographic prescription to evaluate the holographic entanglement entropy through a bulk computation. For static three dimensional gravitational spacetimes and a single interval A in the dual CFT, the RT prescription requires the minimal length curve anchored to the endpoints of A (the RT curve, denoted by γ_A in section 1) because its regularised length multiplied by $1/(4G_{\mathrm{N}})$ provides the holographic entanglement entropy. In a fixed time slice of Poincaré AdS$_3$ and for the interval $A = (-b, b)$, the RT curve is the half circle of radius b centered in the origin (red solid curve in figure 3), whose generic point P_m (that must not be confused with the point indicated in the same way in section 3.2) have coordinates (x_m, ζ_m) satisfying

$$x_m^2 + \zeta_m^2 = b^2 \,. \tag{4.3}$$

It is worth reminding that also the curve $z(\theta = \pi/2, x)$ for $x \in A$ obtained from (3.16) is the half circle centered in the mid-point of A in the complex plane, as already noticed in section 3.3.

Among the holographic bit threads introduced in [35], let us consider the specific configuration given by the geodesic bit threads discussed in [38]. A geodesic bit thread for a RT curve is a geodesic such that it connects a point $x \in A$ to a point that does not belong to A

and intersects the RT curve orthogonally. At such intersection point, its unit norm tangent vector coincides with the unit norm outward-pointing vector normal to the RT curve.

For the RT curve (4.3), the generic geodesic bit thread is (4.2) with [38]

$$R_s = \frac{b\sqrt{b^2 - x_m^2}}{|x_m|} \qquad\qquad x_s = \frac{b^2}{x_m} \qquad\qquad (4.4)$$

where (x_m, ζ_m) are the coordinates of the intersection point between the geodesic bit thread and the RT curve, hence they are constrained by (4.3). Some geodesic bit threads obtained by combining (4.2), (4.3) and (4.4) are shown in figure 3 (green dashed half circles).

We find it more convenient to parameterise a geodesic bit thread in terms of the coordinate $x_A \in A$ of its endpoint in A. The coordinate x_m of the intersection point between the geodesic bit thread and the RT curve is related to x_A as follows[6]

$$x_m = \frac{2\,b^2\,x_A}{b^2 + x_A^2} \qquad\qquad |x_A| \leqslant b \qquad\qquad (4.5)$$

which leads to write (4.4) as

$$R_s = \frac{b^2 - x_A^2}{2\,|x_A|} \qquad\qquad x_s = \frac{b^2 + x_A^2}{2\,x_A} \qquad\qquad (4.6)$$

implying that $(R_s, x_s) = (0, \pm b)$ when $x_A = \pm b$, as expected. From (4.6), one obtains

$$x_s + R_s = \begin{cases} b^2/x_A & x_A > 0 \\ x_A & x_A < 0 \end{cases} \qquad\qquad x_s - R_s = \begin{cases} x_A & x_A > 0 \\ b^2/x_A & x_A < 0\,. \end{cases} \qquad (4.7)$$

Plugging (4.6) into (4.2), we find that the geodesic bit thread anchored to $x_A \in A$ reads

$$\zeta = \sqrt{(x - x_A)\left(\frac{b^2}{x_A} - x\right)} \qquad\qquad |x_A| \leqslant b\,. \qquad\qquad (4.8)$$

From (4.7) or (4.8), we have that the geodesic bit thread intersects the AdS boundary in A at $x = x_A$, as expected by construction, and in the complement of A on the line at $x = x_B$, where

$$x_B = \frac{b^2}{x_A}\,. \qquad\qquad (4.9)$$

This relation between the endpoints of a geodesic bit thread coincides with the inversion relation on the real axis for $t = 0$ provided by the geometric action of the modular conjugation for the interval $A = (-b, b)$, which has been reported in (3.13). Furthermore, let us observe that a geodesic bit thread anchored at $x_A \in A$ (see (4.8) and the green dashed curves in figure 3) and the trajectory corresponding to the Euclidean modular evolution for $\theta \in (0, \pi)$ that starts at the same x_A when $\theta = 0$ (see (3.17) and the black solid curves in figure 2) are described by the same curve. Indeed, they are both half circles whose endpoints are related in the same way. However, these two curves belong to different Euclidean manifolds.

---

[6]The expression (4.5) can be obtained by inverting the relation reported in eq. (2.10) of [38].

Finally, comparing (4.4) and (4.9), we find it worth remarking that the same inversion relation occurs between x_A and x_B and between x_m and x_s.

We remind that the contour function for the entanglement entropies [44, 45] can be associated holographically to the restriction on the boundary of the norm bounded and divergenceless vector field providing the holographic bit threads [46]. In particular, from the vector field for the geodesic bit threads in Poincaré AdS$_3$ found in [38], the function $\beta_0(x)$ for a CFT in the ground state (see (2.4) and (2.5)) is obtained [47].

A straightforward extension of the above analysis allows to address the case of a CFT in the ground state and in the higher dimensional Minkowski spacetime bipartite by a sphere of radius b. For this bipartition it is convenient to adopt the polar coordinates in the Minkowski spacetime with the origin in the center of the sphere. In this case, the geodesic bit threads are obtained from the expressions discussed above restricted to $x > 0$, which corresponds to the radial coordinate.

5 Single interval: thermal state

In this section we consider a CFT in a thermal state at temperature $1/\beta$ and on the line bipartite by an interval $A = (a, b)$ and its complement. This thermal state is the geometric one within the analysis performed in [28, 29], which satisfies the Stefan-Boltzmann law (2.6). In this case the function $w(u)$ to employ is reported in (2.7) [16, 17]. The KMS condition is fulfilled, both in the modular time and in the physical time (see (2.12) and (2.18) respectively).

The geometric action of the modular automorphism group of the diamond induced by the thermal state can be found by specialising (2.9) to (2.7) and the result is [21]

$$\xi(\tau, u) = \frac{\beta}{2\pi} \log\left(\frac{\mathrm{e}^{\pi(b+a)/\beta} + \mathrm{e}^{2\pi b/\beta}\,\mathrm{e}^{w(u)+2\pi\tau}}{\mathrm{e}^{\pi(b-a)/\beta} + \mathrm{e}^{w(u)+2\pi\tau}} \right) \tag{5.1}$$

where $u \in A$ and $\tau \in \mathbb{R}$.

In the Euclidean spacetime, by specialising (2.10) to (2.7), one finds [17]

$$z(\theta, x) = w^{-1}\big(w(x) + \mathrm{i}\theta\big) = \frac{\beta}{2\pi} \log\left(\frac{\mathrm{e}^{\pi(b+a)/\beta} + \mathrm{e}^{2\pi b/\beta}\,\mathrm{e}^{w(x)+\mathrm{i}\theta}}{\mathrm{e}^{\pi(b-a)/\beta} + \mathrm{e}^{w(x)+\mathrm{i}\theta}} \right) \tag{5.2}$$

$$= \frac{\beta}{2\pi} \log\left(\frac{(\mathrm{e}^{2\pi b/\beta} - \mathrm{e}^{2\pi x/\beta})\mathrm{e}^{2\pi a/\beta} + (\mathrm{e}^{2\pi x/\beta} - \mathrm{e}^{2\pi a/\beta})\,\mathrm{e}^{2\pi b/\beta}\,\mathrm{e}^{\mathrm{i}\theta}}{\mathrm{e}^{2\pi b/\beta} - \mathrm{e}^{2\pi x/\beta} + (\mathrm{e}^{2\pi x/\beta} - \mathrm{e}^{2\pi a/\beta})\,\mathrm{e}^{\mathrm{i}\theta}} \right) \tag{5.3}$$

where $x \in A$ and $\theta \in [0, 2\pi)$. In the zero temperature limit $\beta \to +\infty$, the expressions (5.1) and (5.2) become (3.1) and (3.16) respectively, as expected.

In the limiting regime where A becomes the half line, i.e. when $a = 0$ and $b \to +\infty$, one finds that (5.1) simplifies to [23][7]

$$\xi(\tau, x) \longrightarrow \frac{\beta}{2\pi} \log\big[1 + \mathrm{e}^{2\pi\tau}(\mathrm{e}^{2\pi x/\beta} - 1)\big]. \tag{5.4}$$

In the Euclidean spacetime, by taking the same limit in (5.2), we obtain (5.4) with $2\pi\tau$ replaced by $\mathrm{i}\theta$.

---

[7]See eq. (4.14) in [23], with $u_{\text{there}} = \tau_{\text{here}}$ and $f_{\text{there}}(x) = x$.

5.1 Inversion on the real line

By adapting the observation (3.22), made for the ground state, to a CFT at finite temperature and on the bipartite line, from (5.1) or (5.2) we introduce the following inversion map

$$z_{\text{inv}}(x) \equiv \xi(\tau = \text{i}/2 \,, x) = z(\theta = \pi, x) = \frac{\beta}{2\pi} \log\!\left(\frac{\text{e}^{\pi(b+a)/\beta} - \text{e}^{2\pi b/\beta}\,\text{e}^{w(x)}}{\text{e}^{\pi(b-a)/\beta} - \text{e}^{w(x)}}\right). \tag{5.5}$$

In this expression the argument of the logarithm becomes negative for some values of $x \in A$. The range of these values can be found by observing that the denominator and the numerator of the ratio in the argument of the logarithm in (5.5) vanish when x is equal respectively to

$$a_\beta \equiv a + \frac{\ell - \ell_\beta}{2} = a + \frac{\ell}{2}\left(1 - \frac{\log[\cosh(\pi\ell/\beta)]}{\pi\ell/\beta}\right) = -\frac{\beta}{2\pi}\log\!\big[(\text{e}^{-2\pi a/\beta} + \text{e}^{-2\pi b/\beta})/2\big] \tag{5.6}$$

$$b_\beta \equiv b - \frac{\ell - \ell_\beta}{2} = b - \frac{\ell}{2}\left(1 - \frac{\log[\cosh(\pi\ell/\beta)]}{\pi\ell/\beta}\right) = \frac{\beta}{2\pi}\log\!\big[(\text{e}^{2\pi a/\beta} + \text{e}^{2\pi b/\beta})/2\big] \tag{5.7}$$

where

$$\ell_\beta \equiv b_\beta - a_\beta = \frac{\beta}{\pi}\log\!\big[\cosh(\pi\ell/\beta)\big] = \ell + \frac{\beta}{\pi}\log\!\big[(1 + \text{e}^{-2\pi\ell/\beta})/2\big] < \ell \,. \tag{5.8}$$

The argument of the logarithm in (5.5) is negative when $x \in A_\beta$, where $A_\beta \equiv (a_\beta \,, b_\beta)$, which is a proper subinterval of A of length ℓ_β. From (5.6) and (5.7), one observes that A_β and A have the same mid-point. Thus, when $a = -b$, also $a_\beta = -b_\beta$.

From (5.8), we have that $\ell_\beta \to 0$ as $\beta \to +\infty$ and $\ell_\beta \to \ell$ as $\beta \to 0$; namely A_β disappears at zero temperature while it coincides with A in the large temperature regime.

In the limit where A becomes the half-line, which is obtained by setting $b = a + \ell$ first and then taking $\ell \to +\infty$, for the endpoints of A_β in (5.6) and (5.7) we find that $a_\beta \to a + \frac{\beta}{2\pi}\log(2)$ and $b_\beta \to +\infty$ respectively. Now, taking $a \to -\infty$ in this result, A_β becomes the whole line. This is found also by taking $b \to +\infty$ and $a \to -\infty$ simultaneously in (5.6) and (5.7).

Let us stress that A_β has been introduced through the inversion map (5.5). It would be insightful to find a footprint of A_β without invoking the modular conjugation.

Since the argument of the logarithm in (5.5) is negative when $x \in A_\beta$, the inversion (5.5) is a complex map that can be written as follows

$$z_{\text{inv}}(x) = \frac{\beta}{2\pi}\log\!\left(\left|\frac{\text{e}^{\pi(b+a)/\beta} - \text{e}^{2\pi b/\beta}\,\text{e}^{w(x)}}{\text{e}^{\pi(b-a)/\beta} - \text{e}^{w(x)}}\right|\right) \pm \text{i}\,\frac{\beta}{2}\,\Theta_{A_\beta}(x) \tag{5.9}$$

$$= \begin{cases} \dfrac{\beta}{2\pi}\log\!\left(\dfrac{\text{e}^{\pi(b+a)/\beta} - \text{e}^{2\pi b/\beta}\,\text{e}^{w(x)}}{\text{e}^{\pi(b-a)/\beta} - \text{e}^{w(x)}}\right) & x \in A \setminus A_\beta \\[4mm] \dfrac{\beta}{2\pi}\log\!\left(\dfrac{\text{e}^{2\pi b/\beta}\,\text{e}^{w(x)} - \text{e}^{\pi(b+a)/\beta}}{\text{e}^{\pi(b-a)/\beta} - \text{e}^{w(x)}}\right) \pm \text{i}\,\dfrac{\beta}{2} & x \in A_\beta \end{cases} \tag{5.10}$$

where $\Theta_{A_\beta}(x)$ it the characteristic function[8] of A_β. It is worth remarking that the real functions $z_{\text{inv}}(x) : A \setminus A_\beta \to B$ and $\text{Re}[z_{\text{inv}}(x)] : A_\beta \to \mathbb{R}$ are both bijective. They are

---

[8]The characteristic function $\Theta_R(x)$ of a region R is equal to one when $x \in R$ and zero otherwise.
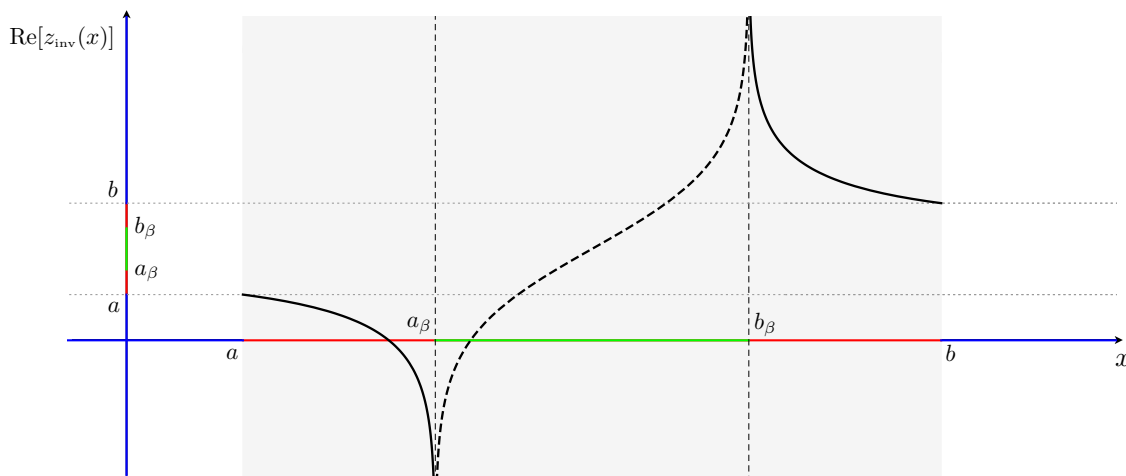
Figure 4. The real part of the inversion map (5.10). The green segment corresponds to A_β, the red segments to $A \setminus A_\beta$ and the blue half lines to B.

shown in figure 4 through the solid curves and the dashed curve respectively. The latter one tells us that $\mathrm{Re}[z_\mathrm{inv}(x)] : A_\beta \to \mathbb{R}$ is strictly increasing.

Combining the two chiralities, in section 5.3 we will see that the imaginary part occurring in the complex map $z_\mathrm{inv}(x) : A_\beta \to \mathbb{R}$ cancels and therefore naturally provides a second Minkowski space $\widetilde{\mathcal{M}}$, which has been called second world in [24] or shadow (virgin) world in [25]. We remark that this second world $\widetilde{\mathcal{M}}$, differently from the real one $\mathcal{M}$, is not bipartite.

In the special case of $A = (-b, b)$, the inversion map (5.10) simplifies to

$$
z_\mathrm{inv}(x) =
\begin{cases}
\dfrac{\beta}{2\pi} \, \log\!\left(\dfrac{\mathrm{e}^{2\pi x/\beta} \cosh(2\pi b/\beta) - 1}{\mathrm{e}^{2\pi x/\beta} - \cosh(2\pi b/\beta)} \right) & x \in A \setminus A_\beta \\[4mm]
\dfrac{\beta}{2\pi} \, \log\!\left(\dfrac{\mathrm{e}^{2\pi x/\beta} \cosh(2\pi b/\beta) - 1}{\cosh(2\pi b/\beta) - \mathrm{e}^{2\pi x/\beta}} \right) \pm \mathrm{i}\, \dfrac{\beta}{2} & x \in A_\beta \, .
\end{cases}
\tag{5.11}
$$

This result will be re-obtained holographically also through the geodesic bit threads in the BTZ black brane background in section 6.

In the zero temperature limit $\beta \to +\infty$, we have that $A_\beta \to \emptyset$, as remarked above; hence only the first expression in (5.10) must be considered, which becomes (3.8) in this limit, as expected.

In the limiting regime $b \to +\infty$, the interval A becomes the half-line $(a, +\infty)$ and, by using also the above results $a_\beta \to a + \frac{\beta}{2\pi} \log(2)$ and $b_\beta \to +\infty$, one finds that the map (5.10) simplifies to

$$
z_\mathrm{inv}(x) =
\begin{cases}
a + \dfrac{\beta}{2\pi} \, \log\!\left(2 - \mathrm{e}^{2\pi(x-a)/\beta} \right) & a < x < a + \dfrac{\beta}{2\pi} \log(2) \\[4mm]
a + \dfrac{\beta}{2\pi} \, \log\!\left(\mathrm{e}^{2\pi(x-a)/\beta} - 2 \right) \pm \mathrm{i}\, \dfrac{\beta}{2} & x > a + \dfrac{\beta}{2\pi} \log(2)
\end{cases}
\tag{5.12}
$$

which is real in $A \setminus A_\beta = (a, a + \frac{\beta}{2\pi} \log(2))$ and sends this limited interval onto the half line $B = (-\infty, a)$ complementary to A in a bijective way. By employing the exponential map characterising the thermal state, we can write (5.12) in the following suggestive form

$$\mathrm{e}^{2\pi[z_{\mathrm{inv}}(x)-a]/\beta} = 2 - \mathrm{e}^{2\pi(x-a)/\beta} \tag{5.13}$$

which becomes (3.15) in the zero temperature limit, as expected. In the non negative variable $y \equiv \mathrm{e}^{2\pi(x-a)/\beta}$, this map becomes to the reflection $y \to 2 - y$ with respect to 1. The reflection (5.13) suggests to continue this real positive variable y by including also the semi-axis made by the negative real numbers $y < 0$, which corresponds to the second world [24, 25]. Indeed, such reflection maps the points $y > 2$ into the negative real semi-axis in a bijective way.

In order to explore the meaning of the sub-interval A_β, we find it worth exploiting the contour function for the entanglement entropies [44, 45]. For a CFT at finite temperature on the line bipartite by an interval, this function reads [45][9]

$$s_A^{(n)}(x) \equiv \frac{c}{12}\left(1 + \frac{1}{n}\right) w'(x) + \frac{C}{\ell} \tag{5.14}$$

where $w(x)$ is given by (2.7) and C is a non universal constant such that $s_A^{(n)}(x) > 0$ for every $x \in A$. The main feature of the positive function (5.14) is that the entanglement entropies of A found in [48] are obtained by integrating it on $A_\epsilon \equiv (a + \epsilon, b - \epsilon)$, where ϵ is the UV cutoff, i.e.

$$S_A^{(n)} = \int_{a+\epsilon}^{b-\epsilon} s_A^{(n)}(x)\,\mathrm{d}x = \frac{c}{12}\left(1 + \frac{1}{n}\right)\log\left[\frac{\beta}{\pi\epsilon}\sinh(\pi\ell/\beta)\right] + O(1) \tag{5.15}$$

up to $O(1)$ non universal contributions as $\epsilon \to 0$. In [48] it has been remarked that, when $\ell \gg \beta$, the entanglement entropy obtained from (5.15) becomes extensive and provides the Gibbs entropy $S_A \simeq \pi c \ell/(3\beta)$ of an isolated system of length ℓ coming from the Stefan-Boltzmann law for a 2D CFT (see (2.6)) [43, 49, 50].

It is sometimes insightful to integrate the contour function for the entanglement entropies in (5.14) over a subsystem properly included in A (see e.g. [51]). In the case that we are exploring, the integration of (5.14) over A_β gives

$$\int_{a_\beta}^{b_\beta} s_A^{(n)}(x)\,\mathrm{d}x = \frac{c}{12}\left(1 + \frac{1}{n}\right)\left[w(b_\beta) - w(a_\beta)\right] + \frac{C}{\ell}\ell_\beta = \frac{c}{6}\left(1 + \frac{1}{n}\right)\frac{\pi\ell}{\beta} + \frac{\ell_\beta}{\ell}C. \tag{5.16}$$

where ℓ_β has been introduced in (5.8). When $n = 1$ and $C = 0$, the expression (5.16) provides the above mentioned Gibbs entropy $\pi c \ell/(3\beta)$ for any value of ℓ and β.

Considering the sub-interval A_β, from (2.7) and its endpoints (5.6) and (5.7), one finds

$$w(b_\beta) - w(a_\beta) = \frac{2\pi(b-a)}{\beta} \equiv \tau_\beta \tag{5.17}$$

which can be interpreted through the modular parameter τ. Indeed, by considering (2.9) for $x = a_\beta$, the expression (5.17) corresponds to the value τ_β of the modular parameter such that $\xi(\tau_\beta, a_\beta) = b_\beta$. As a consequence, also (5.16) can be interpreted through the modular parameter τ because it is proportional to (5.17) when $C = 0$.

---

[9]See eqs. (65) and (71) of [45].
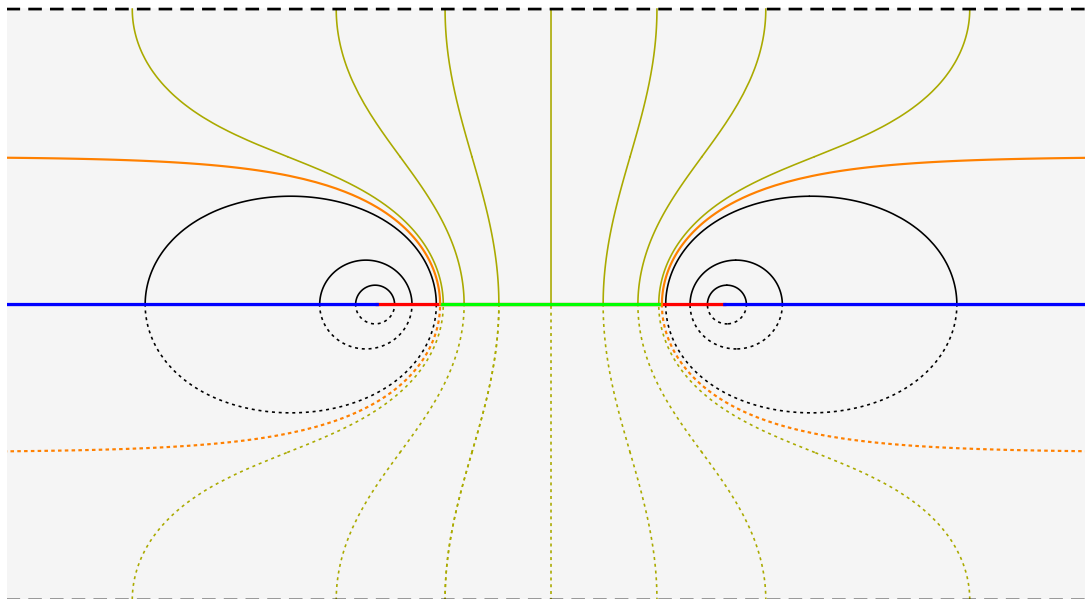
Figure 5. Euclidean modular evolution for a CFT at finite temperature $1/\beta$ on the bipartite line, obtained from (5.2), with $\theta \in (0, \pi)$ (solid arcs) or $\theta \in (\pi, 2\pi)$ (dotted arcs), for some $x \in A$. The green segment corresponds to A_β. The solid black curves (or the dotted black ones equivalently) map $A \setminus A_\beta$ into B in a bijective way, while the solid yellow curves (or the dotted yellow ones equivalently) map A_β into the horizontal dashed black line at $\mathrm{Im}(z) = +\beta/2$ (which is identified with the horizontal dashed black line at $\mathrm{Im}(z) = -\beta/2$) in a bijective way.

5.2 Geometric action in Euclidean spacetime

In the finite temperature case that we are investigating, the geometric action of the modular conjugation can be studied by adapting the observations made in section 3.2 and section 3.3 for the ground state. It is more instructive to discuss first the Euclidean spacetime.

For a CFT at finite temperature $1/\beta$ on the line, the Euclidean spacetime to consider is the infinite cylinder whose section along the compactified direction is a circle having length equal to β. It can be equivalently represented by the horizontal strip $\{z \in \mathbb{C}; |\mathrm{Im}(z)| \leqslant \beta/2\}$ in the complex plane (parameterised by z) with vertical width equal to β (grey region in figure 5), where the horizontal lines at $\mathrm{Im}(z) = \pm\beta/2$ delimiting the strip (horizontal black dashed lines in figure 5) are identified. The space where the CFT is defined corresponds to the real axis $\mathrm{Im}(z) = 0$, which is bipartite by the interval A and its complement. This bipartition is characterised by the entangling points $x = a$ and $x = b$ on the real axis, which correspond to the points where a red segment and a blue segment join in figure 5; hence A is the union of the two red segments and the green segment, while B corresponds to the union of the two blue half lines.

The curves shown in figure 5 are obtained from (5.2) for some values of $x \in A$: the solid ones have $\theta \in (0, \pi)$, while $\theta \in (\pi, 2\pi)$ for the dotted ones. Any black solid arc (or equivalently the dotted one having the same endpoints) associates a point in the red segments to a point in B in a unique way. Instead, any yellow arc (or equivalently the dotted one having the same endpoints) associates a point in the green segment to a point

on the horizontal black dashed lines at $\text{Im}(z) = \pm\beta/2$ (which are identified). This map is (5.10) and the green segment in figure 5 denotes the sub-interval A_β. The two orange curves in figure 5 intersect the real axis at $x = a_\beta$ or $x = b_\beta$ and connect these points to $-\infty$ or $+\infty$ respectively; hence they provide the extremal lines separating the set of the black curves and the set of the yellow curves, whose behaviours are qualitatively different. In this Euclidean setup, the horizontal black dashed lines at $\text{Im}(z) = \pm\beta/2$ corresponds to the space of the second world [24, 25] introduced in section 5.1.

In this Euclidean strip, it is useful to consider also the curves obtained from (5.2) at fixed $\theta \in (0, 2\pi)$, parameterised by $x \in A$. For these curves, we find that $\partial_x z(\theta, x) \to e^{i\theta}$ as $x \to a$ and $\partial_x z(\theta, x) \to e^{-i\theta}$ as $x \to b$; hence the curve corresponding to $\theta = \pi/2$ intersects orthogonally the real axis at $x = a$ and $x = b$. This result is independent of β and for the ground state it has been already remarked in section 3.3.

5.3 Geometric action in Minkowski spacetime

In the Minkowski spacetime $\mathcal{M}$ parameterised by the coordinates (x, t), let us consider the diamond $\mathcal{D}_A$ (see section 3.1). The occurrence of the sub-interval A_β introduced in section 5.1, whose endpoints on the spatial line are (5.6) and (5.7), naturally leads to the following partition

$$\mathcal{D}_A = \mathcal{D}_{A_\beta} \cup \widetilde{\mathcal{D}}_A \cup \mathcal{R}_A \qquad (5.18)$$

identified by the null rays departing from the points $(a_\beta, 0)$ and $(b_\beta, 0)$ (see figure 6). In (5.18), $\mathcal{D}_{A_\beta}$ is the domain of dependence (diamond) of A_β (green region in figure 6), while $\widetilde{\mathcal{D}}_A$ and $\mathcal{R}_A$ are defined as follows

$$\widetilde{\mathcal{D}}_A \equiv \widetilde{\mathcal{D}}_{\text{R}} \cup \widetilde{\mathcal{D}}_{\text{L}} \cup \widetilde{\mathcal{D}}_{\text{F}} \cup \widetilde{\mathcal{D}}_{\text{P}} \qquad \mathcal{R}_A \equiv \mathcal{R}_{++} \cup \mathcal{R}_{-+} \cup \mathcal{R}_{--} \cup \mathcal{R}_{+-} \, . \qquad (5.19)$$

The domains $\widetilde{\mathcal{D}}_k$ with $k \in \{\text{R}, \text{L}, \text{F}, \text{P}\}$ are the dark grey diamonds in figure 6 and the letters for the subindex, which stand for right, left, future and past respectively (see also (3.2)), indicate their position with respect to $\mathcal{D}_{A_\beta}$. Each of these diamonds shares a vertex with $\mathcal{D}_{A_\beta}$. The domains $\mathcal{R}_{rs}$ with $r, s \in \{+, -\}$ are the light grey rectangles in figure 6 and the subindices indicate their position with respect to $\mathcal{D}_{A_\beta}$ (e.g. $++$ and $+-$ correspond to the top right and top left light grey rectangle respectively).

In the limit where A becomes the half line, $\mathcal{D}_A$ and $\mathcal{D}_{A_\beta}$ become the right wedges with vertex in $(a, 0)$ and $(a + \frac{\beta}{2\pi} \log(2), 0)$ respectively. Furthermore, only $\widetilde{\mathcal{D}}_{\text{L}}$ remains a finite diamond in this limit, while the other dark grey regions $\widetilde{\mathcal{D}}_k$ with $k \neq \text{L}$ disappear at infinity.

In the zero temperature limit $\beta \to +\infty$, we have that $\mathcal{D}_{A_\beta}$ and $\mathcal{R}_A$ become zero measure regions in Minkowski space and $\widetilde{\mathcal{D}}_A \to \mathcal{D}_A$. Moreover, considering the partitions of $\mathcal{D}_A$ introduced in (3.2) and (5.19), in this limit we have that $\widetilde{\mathcal{D}}_k \to \mathcal{D}_k$ for each $k \in \{\text{R}, \text{L}, \text{F}, \text{P}\}$, up to zero measure domains.

A modular trajectory in Minkowski space is obtained by combining (5.1) and (2.20). It depends on the assigned value $x \in A$ at $\tau = 0$ and it entirely belongs to $\mathcal{D}_A$. The partition (5.18) of $\mathcal{D}_A$ induces a partition of a modular trajectory into (at most) five arcs corresponding to its intersections with $\mathcal{D}_{A_\beta}$, $\widetilde{\mathcal{D}}_A$ and $\mathcal{R}_A$ (arcs denoted with different colours that partition each solid curve in figure 6). The only exception is the modular trajectory
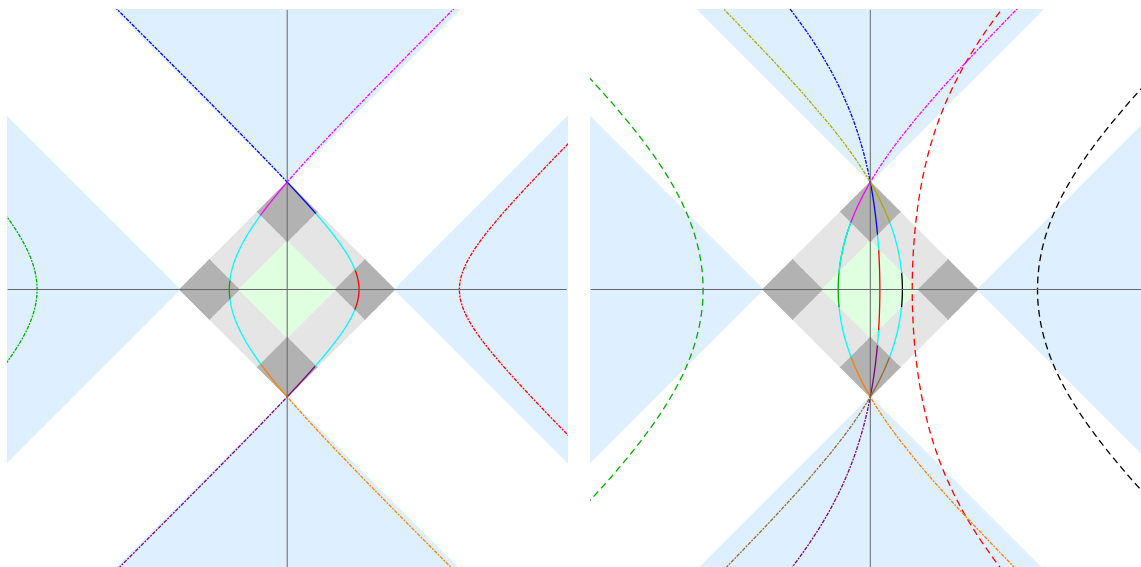
Figure 6. Modular trajectories (solid lines) in $\mathcal{D}_A$ passing at some $x \in A$ when $t = 0$ and their images (dot-dashed and dashed lines) under (5.23). Left: two values of $x \in A \setminus A_\beta$. Right: three values of $x \in A_\beta$. The arcs denoted through different kind of lines but having the same colour are related through (5.23). While the dot-dashed lines span $\mathcal{W}_A$ (light blue region, see (3.9)) as $x \in A \setminus A_\beta$, the dashed lines span the entire Minkowski spacetime (the second world $\widetilde{\mathcal{M}}$) as $x \in A_\beta$.

corresponding to $x = \frac{a+b}{2}$, which is the vertical segment connecting the top and bottom vertices of $\mathcal{D}_A$; indeed, its partition is made only by three vertical segments because it does not intersect $\mathcal{R}_A$. The five arcs partitioning the modular trajectory can be found also through the corresponding values of the modular parameter. The ranges of τ that provide the different arcs are identified by $\pm|\tau_{a_\beta}|$ and $\pm|\tau_{b_\beta}|$, where

$$\tau_{a_\beta} \equiv \frac{w(a_\beta) - w(x)}{2\pi} \qquad \tau_{b_\beta} \equiv \frac{w(b_\beta) - w(x)}{2\pi} \,. \qquad (5.20)$$

A modular trajectory is characterised by its point $(x, 0)$ with $x \in A$ at $\tau = 0$. At finite temperature, we have either $x \in A \setminus A_\beta$ (left panel in figure 6) or $x \in A_\beta$ (right panel in figure 6). Considering the partition (5.18), notice that, while all the modular trajectories have non vanishing intersections with $\widetilde{\mathcal{D}}_A$ ad $\mathcal{R}_A$, only those ones corresponding to $x \in A_\beta$ intersect also $\mathcal{D}_{A_\beta}$.

In order to adapt to the thermal case the results discussed in section 3.2 for the ground state (see (3.3) and (3.5)), we introduce the geometric action of the modular conjugation as follows

$$x_{\text{inv}}(x, t) = \frac{z_{\text{inv}}(x + t) + z_{\text{inv}}(x - t)}{2} \qquad t_{\text{inv}}(x, t) = \frac{z_{\text{inv}}(x + t) - z_{\text{inv}}(x - t)}{2} \qquad (5.21)$$

where the function $z_{\text{inv}}(x)$ is given by (5.9). In terms of the light ray coordinates (2.1), it is convenient to introduce $u_{\pm,\text{inv}} \equiv x_{\text{inv}} \pm t_{\text{inv}}$, finding that

$$u_{\pm,\text{inv}} = z_{\text{inv}}(u_\pm) \,. \qquad (5.22)$$

From (5.21) we obtain

$$
\begin{cases}
x_{\text{inv}}(x,t) \;=\; \dfrac{\beta}{4\pi}\,\log\!\left[\dfrac{\big(\mathrm{e}^{\pi(b+a)/\beta}-\mathrm{e}^{2\pi b/\beta}\,\mathrm{e}^{w(x+t)}\big)\big(\mathrm{e}^{\pi(b+a)/\beta}-\mathrm{e}^{2\pi b/\beta}\,\mathrm{e}^{w(x-t)}\big)}{\big(\mathrm{e}^{\pi(b-a)/\beta}-\mathrm{e}^{w(x+t)}\big)\big(\mathrm{e}^{\pi(b-a)/\beta}-\mathrm{e}^{w(x-t)}\big)}\right] \\[1.2em]
t_{\text{inv}}(x,t) \;=\; \dfrac{\beta}{4\pi}\,\log\!\left[\dfrac{\big(\mathrm{e}^{\pi(b+a)/\beta}-\mathrm{e}^{2\pi b/\beta}\,\mathrm{e}^{w(x+t)}\big)\big(\mathrm{e}^{\pi(b-a)/\beta}-\mathrm{e}^{w(x-t)}\big)}{\big(\mathrm{e}^{\pi(b-a)/\beta}-\mathrm{e}^{w(x+t)}\big)\big(\mathrm{e}^{\pi(b+a)/\beta}-\mathrm{e}^{2\pi b/\beta}\,\mathrm{e}^{w(x-t)}\big)}\right].
\end{cases}
\tag{5.23}
$$

This map satisfies some consistency relations. For $t=0$ we have $t_{\text{inv}}(x,t=0)=0$, as expected, and, interestingly, $x_{\text{inv}}(x,t=0)=\mathrm{Re}[z_{\text{inv}}(x)]$, which is shown in figure 4. In the zero temperature limit $\beta\to+\infty$, the inversion map (3.3) is recovered, as expected. We remark that (5.23) has been obtained by merging the two logarithmic functions coming from $z_{\text{inv}}(x+t)$ and $z_{\text{inv}}(x-t)$ into a single logarithmic function and that such seemingly innocent simplification leads to interesting consequences, as discussed below.

Consider the partitions in (5.18) and (5.19), together with the partition (3.9) for the light blue region in both panels of figure 6. When $(x,t)\in\widetilde{\mathcal{D}}_A$, the inversion map (5.21) is equivalent to (5.23) and it defines the four bijective maps $\widetilde{\mathcal{D}}_{\text{R}}\to\mathcal{W}_{\text{R}}$, $\widetilde{\mathcal{D}}_{\text{L}}\to\mathcal{W}_{\text{L}}$, $\widetilde{\mathcal{D}}_{\text{F}}\to\mathcal{V}_{\text{F}}$ and $\widetilde{\mathcal{D}}_{\text{P}}\to\mathcal{V}_{\text{P}}$.

The action of the map (5.23) in $\mathcal{D}_{A_\beta}$ and $\mathcal{R}_A$ is very interesting. When $(x,t)\in\mathcal{D}_{A_\beta}$, the arguments of the logarithm in $z_{\text{inv}}(x+t)$ and $z_{\text{inv}}(x-t)$ are both negative; hence (5.21) gives $\mathrm{Im}(t_{\text{inv}})=0$ and $|\mathrm{Im}(x_{\text{inv}})|=\beta/2$. Instead, in (5.23) the arguments of the logarithms remains positive; hence (5.23) is a real map from $\mathcal{D}_{A_\beta}$ to the entire Minkowski spacetime $\widetilde{\mathcal{M}}$, which is identified with the second world. This is an interesting consequence of the combination of the two different chiralities; indeed, they separately provide results with non vanishing imaginary parts. Notice that, differently from $\mathcal{M}$, the space direction of $\widetilde{\mathcal{M}}$ is not bipartite. In the right panel of figure 6, a dashed curve of certain colour is the image under (5.23) of the solid arc in $\mathcal{D}_{A_\beta}$ having the same colour. As $x\in A_\beta$, these dashed curves span the entire Minkowski spacetime $\widetilde{\mathcal{M}}$ (the second world). Hence, *the structure of the "real world" is transported with the help of the conjugation J to the "second world"*, as Borchers observed in [24].

The above discussion tells us that the full modular Hamiltonian in $\mathcal{M}\cup\widetilde{\mathcal{M}}$ reads

$$
K = K_A\otimes\mathbf{1}_{B\cup\widetilde{\mathcal{M}}}-\mathbf{1}_A\otimes JK_AJ.
\tag{5.24}
$$

In the zero temperature limit $\beta\to+\infty$, we have that the second world $\widetilde{\mathcal{M}}$ disappears and (5.24) tends to $K=K_A\otimes\mathbf{1}_B-\mathbf{1}_A\otimes K_B$, where $K_B=JK_AJ$, being J the modular conjugation whose geometric action has been described in section 3.

Instead, the image of a point $(x,t)\in\mathcal{R}_A$ under (5.21) or (5.23) has $|\mathrm{Im}(t_{\text{inv}})|=|\mathrm{Im}(x_{\text{inv}})|=\beta/4$; hence the reality condition suggest to consider this result unphysical. In figure 6, this implies that the cyan arcs do not have a dot-dashed or dashed counterpart.

When A becomes the half line, i.e. in the limit $b \to +\infty$, the inversion (5.23) simplifies to

$$\begin{cases} x_{\text{inv}}(x,t) = a + \dfrac{\beta}{4\pi} \log\Big[\big(e^{2\pi(x-a+t)/\beta} - 2\big)\big(e^{2\pi(x-a-t)/\beta} - 2\big)\Big] \\[4mm] t_{\text{inv}}(x,t) = \dfrac{\beta}{4\pi} \log\bigg(\dfrac{e^{2\pi(x-a+t)/\beta} - 2}{e^{2\pi(x-a-t)/\beta} - 2}\bigg) \end{cases} \tag{5.25}$$

whose zero temperature limit gives (3.14), as expected.

In terms of the light ray coordinates $u_\pm$ and of $u_{\pm,\text{inv}} \equiv x_{\text{inv}} \pm t_{\text{inv}}$, the map (5.25) can be written in the form (5.12) or (5.13), as expected.

6 Geodesic bit threads in BTZ black brane

In this section we show that the inversion map on the real line discussed in section 5.1 can be found through the geodesic bit threads in the BTZ black brane geometry described in [38].

The BTZ black brane is a three dimensional gravitational background solving the Einstein equations with negative cosmological constant and without matter term. A horizon occurs and it is a two dimensional plane. This geometry can be described in terms of the coordinates (t, x, ζ), where t is the time coordinate and $\zeta > 0$ is the holographic coordinate. The boundary at $\zeta = 0$ is a $1+1$ dimensional Minkowski spacetime $\mathcal{M}$ in the coordinates (x, t). A constant time slice of the BTZ black brane geometry is equipped with the following induced metric

$$ds^2 = \frac{1}{\zeta^2}\left(dx^2 + \frac{d\zeta^2}{1 - (\zeta/\zeta_h)^2}\right) \qquad\qquad \zeta > 0 \tag{6.1}$$

where ζ_h denotes the position of the horizon. This two dimensional geometry is considered in figure 7, where the yellow region corresponds to $0 < \zeta < \zeta_h$ and the grey region to $\zeta > \zeta_h$. The AdS/CFT correspondence relates ζ_h to the temperature $1/\beta$ of the dual 2D CFT in the Minkowski spacetime at the boundary of the BTZ black brane as follows

$$\zeta_h = \frac{\beta}{2\pi}\,. \tag{6.2}$$

Consider the bipartition of the spatial line of the dual CFT given by an interval, which can be set to $A = (-b, b) \subset \mathbb{R}$ without loss of generality (see the union of the red segments and of the green segment in figure 7, while the union of the blue half lines is the complement of A on the line), as already done in section 4. In the geometry (6.1), the minimal length curve anchored to the endpoints of A (the RT curve) is made by the points P_m (that must not be confused with the point indicated in the same way in section 3.2) whose coordinates (x_m, ζ_m) satisfy the following constraint

$$\zeta_m = \sqrt{\frac{\zeta_h^2 + \zeta_*^2}{2} - \frac{\zeta_h^2 - \zeta_*^2}{2}\,\cosh(2x_m/\zeta_h)} = \zeta_h\,\frac{\sqrt{\cosh(2b/\zeta_h) - \cosh(2x_m/\zeta_h)}}{\sqrt{2}\,\cosh(b/\zeta_h)} \tag{6.3}$$

where ζ_* denotes the maximum depth of this geodesic, which can be expressed in terms of ζ_h and b as follows

$$\zeta_* = \zeta_h \tanh(b/\zeta_h)\,. \tag{6.4}$$
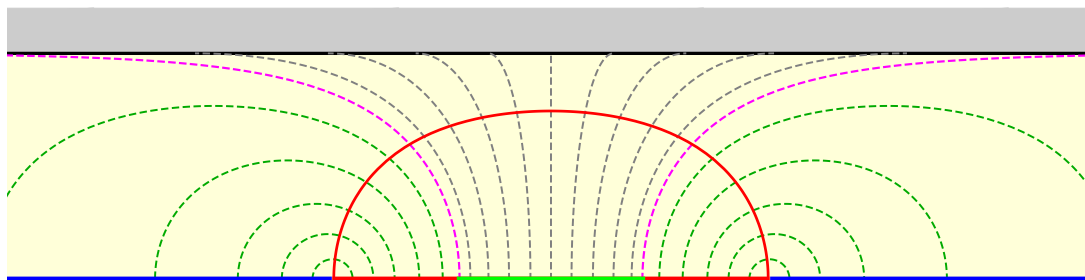
Figure 7. Geodesic bit threads in BTZ black brane geometry for an interval on the line. The red solid curve is the RT curve (6.3). The green segment corresponds to A_β (see section 5.1).

In figure 7, the RT curve (6.3) corresponds to the red solid curve in the yellow region. This RT curve does not coincide with the one discussed in the last paragraph of section 5.2. These two curves overlap in the zero temperature limit, as remarked in section 4.

The geodesic bit threads for the BTZ black brane geometry (6.1) and the RT curve (6.3) have been found in [38]. In the following we report some of their results, trying to keep their notation wherever it is possible.

Some geodesic bit threads (dashed lines) are shown in figure 7 (see also the left panel of figure 4 in [38]). A crucial feature of these geodesic bit threads is that those ones whose intersection with the RT curve (6.3) has x_m such that $x_{m,\max} < |x_m| < b$ with

$$x_{m,\max} \equiv \zeta_h \operatorname{arccoth}(\zeta_h^2/\zeta_*^2) \qquad (6.5)$$

have both the endpoints on the boundary at $\zeta = 0$; hence they connect a point A to a point in its complement B on the line (green dashed curves in figure 7). Instead, the geodesic bit threads intersecting the RT curve (6.3) in a point whose coordinate x_m satisfies $|x_m| \leqslant x_{m,\max}$ reach the horizon; hence they connect a point in A to a point on the horizon (grey dashed curves in figure 7).

A convenient parameterisation for the geodesic bit threads connecting A to its complement on the real axis is

$$\zeta = \sqrt{C_1 + C_2 \cosh[2(x - x_m)/\zeta_h] + C_3 \sinh[2(x - x_m)/\zeta_h]} \qquad (6.6)$$

where the constants C_1, C_2 and C_3 are defined respectively as

$$C_1 \equiv \frac{(\zeta_h^2 + \zeta_m^2)(\zeta_h^2 - \zeta_m^2) + \zeta_h^2 \zeta_m^2 s_m^2}{2(\zeta_h^2 - \zeta_m^2)} \qquad C_2 \equiv -\frac{(\zeta_h^2 - \zeta_m^2)^2 + \zeta_h^2 \zeta_m^2 s_m^2}{2(\zeta_h^2 - \zeta_m^2)} \qquad C_3 \equiv \zeta_h \zeta_m s_m \qquad (6.7)$$

being s_m the slope of the outward-pointing normal vector at a given point (x_m, ζ_m) of the RT curve (6.3), that reads

$$s_m \equiv \frac{\zeta_m}{\zeta_h} \coth(x_m/\zeta_h) = \pm \frac{\zeta_m}{\zeta_h} \sqrt{\frac{\zeta_h^2 - \zeta_m^2}{\zeta_*^2 - \zeta_m^2}}. \qquad (6.8)$$

As for the geodesic bit threads connecting a point in A to a point of the horizon, they can be written also as

$$x = x_m + \sigma \, \zeta_h \, \log\left(\frac{\sqrt{\zeta_h^2 - \zeta^2} + \sqrt{D_1^2 + \zeta_m^2 - \zeta^2}}{\sqrt{\zeta_h^2 - \zeta_m^2} - \sigma \, D_1} \right) \tag{6.9}$$

being the constants D_1 and σ defined as follows

$$D_1 \equiv \frac{\zeta_h \, \zeta_m \, s_m}{\sqrt{\zeta_h^2 - \zeta_m^2}} \qquad \sigma \in \{+1, -1\} \tag{6.10}$$

where σ and s_m must have opposite signs. Both the parameterisations (6.6) and (6.9) can be adopted to describe each one of the two different types of geodesic bit threads, by employing two branches if necessary.

In figure 7 we show some geodesic bit threads (dashed lines in the yellow region): the green dashed lines connect a point in A to a point in B, hence both these points are on the boundary; instead, the grey ones connect a point in A to a point on the horizon. The magenta dashed curves denote the geodesic bit threads corresponding to the transition between these two different behaviours, hence they intersect the horizon (or the boundary) at infinity.

The thermal sub-interval $A_\beta \subset A$ introduced in section 5.1, whose endpoints are (5.6) and (5.7), can be found also through the geodesic bit threads in the BTZ black brane geometry described above. Consider the transition geodesic bit thread given by (6.9) with $\sigma = -1$ (hence $s_m > 0$) and having $x_m = x_{m,\mathrm{max}}$ in (6.5), which corresponds to the magenta dashed curve on the right in figure 7. Setting $\zeta = 0$ in the resulting expression, we recover b_β in (5.7) in the special case of $a = -b$. Because of the symmetry of A, the magenta dashed curve on the left in figure 7 provides a_β in (5.6) when $a = -b$. Thus, the green segment on the boundary in figure 7, obtained holographically through the geodesic bit threads corresponding to the magenta dashed curves, can be identified with A_β, which is also the green segment on the real line in figure 5 and the segment on the real axis providing the green diamond in figure 6.

Plugging the expression for ζ_* in (6.4) into (6.5) and comparing the result with b_β in (5.7) specialised to the case $a = -b$, we observe that

$$x_{m,\mathrm{max}} = b_{\frac{\beta}{2}} \, . \tag{6.11}$$

This interesting holographic relation deserves some interpretation.

Also the inversion map (5.11) can be interpret through the geodesic bit threads.

Consider first a point on the boundary at $x_A \in A \setminus A_\beta$, which is therefore connected through a geodesic bit thread described by (6.6) to another point on the boundary at some $x_B \in B$. In order to find x_B in terms of x_A, notice that (6.6) vanishes for $x = x_\pm$ given by

$$x_\pm = x_m + \frac{\zeta_h}{2} \, \log\left(\frac{C_1 \pm \sqrt{C_1^2 - C_2^2 + C_3^2}}{-C_2 - C_3} \right) \tag{6.12}$$
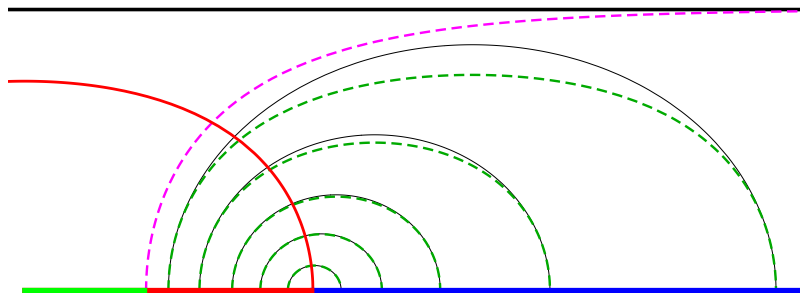
Figure 8. Comparison between geodesic bit threads (green dashed curves) connecting a point $x_A \in A \setminus A_\beta$ to a point $x_B \in B$ (see also figure 7) and the corresponding lines (starting at the same x_A's) for the modular evolution in the Euclidean spacetime described in section 5.2 (black solid curves, see also figure 5).

where, from (6.7), we have

$$-C_2-C_3 = \frac{\left(\zeta_h^2 - \zeta_h\,\zeta_m\,s_m - \zeta_m^2\right)^2}{2\left(\zeta_h^2 - \zeta_m^2\right)} \qquad C_1^2-C_2^2+C_3^2 = \frac{\zeta_h^2\,\zeta_m^2\left[\left(1+s_m^2\right)\zeta_h^2 - \zeta_m^2\right]}{\zeta_h^2 - \zeta_m^2}\,. \quad (6.13)$$

Since $\zeta_h > \zeta_m$, the constant C_1 and both the expressions in (6.13) are positive quantities; hence one concludes that $x_+ > x_-$, from (6.12). The symmetric choice of A with respect to the origin allows us to assume $x_A > b_\beta > 0$ without loss of generality; hence $x_A = x_-$ and $x_B = x_+$ (see figure 8).

To express x_m in terms of $x_A = x_-$, first employ (6.8) and then (6.3) into x_- given by (6.12); and finally invert the resulting expression. This gives different solutions, but the one providing (4.5) when $\zeta_h \to +\infty$ reads

$$x_m = \frac{\zeta_h}{2}\,\log\!\left(\frac{\mathrm{e}^{2x_A/\zeta_h}\big(\mathrm{e}^{4b/\zeta_h}+1\big)+2\,\mathrm{e}^{2b/\zeta_h}-2\,\mathrm{e}^{(b+x_A)/\zeta_h}\big(\mathrm{e}^{2b/\zeta_h}+1\big)}{2\,\mathrm{e}^{2(x_A+b)/\zeta_h}+\mathrm{e}^{4b/\zeta_h}+1-2\,\mathrm{e}^{(b+x_A)/\zeta_h}\big(\mathrm{e}^{2b/\zeta_h}+1\big)}\right). \quad (6.14)$$

Now x_B can be written in terms of x_A by first using (6.8) and (6.3) into $x_+ = x_B$ given by (6.12), and then employing (6.14) in the resulting formula. After some algebra, we obtain

$$\mathrm{e}^{2x_B/\zeta_h} = \left(\frac{\mathrm{e}^{x_A/\zeta_h}\cosh(b/\zeta_h) - 1}{\mathrm{e}^{x_A/\zeta_h} - \cosh(b/\zeta_h)}\right)^2 \quad (6.15)$$

where the ratio within the round brackets in the r.h.s. is positive when $x_A \in A \setminus A_\beta$. Thus, the CFT result (5.11) in $A \setminus A_\beta$ has been obtained holographically through the geodesic bit threads. As consistency check, notice that the limit $\zeta_h \to +\infty$ of the expression for x_B obtained from (6.15) when $x_A \in A \setminus A_\beta$ leads to (4.9), as expected.

In figure 8, considering only the positive half real axis without loss of generality, we show some geodesic bit threads having both the endpoints on the boundary (green dashed curves). These bit threads are compared with the corresponding curves (black solid lines) starting at the same values of $x_A \in A \setminus A_\beta$ obtained from the CFT expression (5.2) for the same value of β, which have been shown also in figure 5. We remark that these two sets of curves belong to two different Euclidean manifolds. These geodesic bit threads
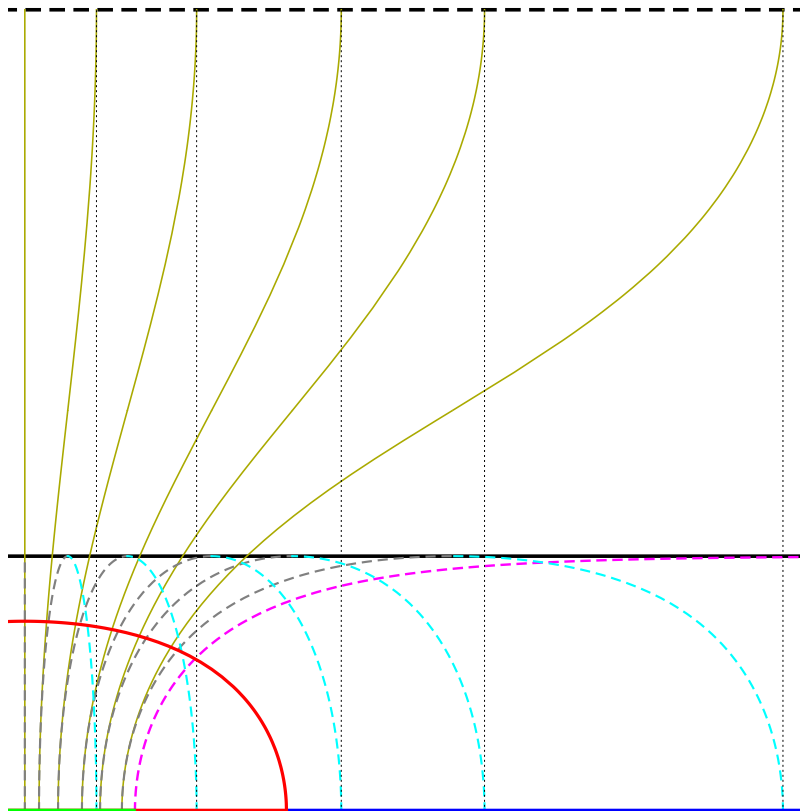
Figure 9. Comparison between geodesic bit threads (grey dashed curves) connecting a point $x_A \in A_\beta$ to a point on the horizon (see also figure 7) and the corresponding lines (starting at the same x_A's) of the modular evolution in the Euclidean spacetime (yellow solid curves, see also figure 5).

share the same endpoints with the corresponding CFT lines, as expected from the analytic result discussed above, but they do not coincide for the other points in general. There is no reason to expect such overlap. However, the overlap approximatively occurs for the geodesics bit threads close to the boundary, which connect points close to the entangling point b. Indeed, since these geodesics bit threads are weakly influenced by the occurrence of the horizon, they become approximatively half circles, i.e. geodesics in Poincaré AdS$_3$.

The inversion map (5.11) obtained from CFT can be recovered holographically through the geodesic bit threads also when $x_A \in A_\beta$. The geodesic bit thread starting at this point on the boundary reaches the horizon at some point (x_h, ζ_h) (grey dashed curves in figure 7 and figure 9). We observe that this bit thread is tangent to the horizon; indeed, from (6.9) one obtains $\partial_\zeta x = -\sigma \zeta_h \zeta \left[(\zeta_h^2 - \zeta^2)(D_1^2 + \zeta_m^2 - \zeta^2) \right]^{-1/2}$, which diverges as $\zeta \to \zeta_h$. Such observation suggests us to merge this geodesic bit thread with the geodesic starting at (x_h, ζ_h) tangentially to the horizon and ending at some point $(\tilde{x}, 0)$ on the boundary (cyan dashed curves in figure 9). The latter geodesic can be obtained by reflecting the geodesic bit thread starting at $(x_A, 0)$ with respect to the vertical axis at $x = x_h$. This construction implies that $\tilde{x} = x_A + 2(x_h - x_A)$. We remark that, because of the singular behavior of the metric in the limit $\zeta \to \zeta h$, the flux of the geodesic bit threads through the whole horizon

does not vanish; indeed, it must be equal to the flux of the geodesic bit threads through (a_β, b_β) at the boundary.

The same procedure described above to obtain x_B from $x_A \in A \setminus A_\beta$ can be employed to find $\tilde{x}$ in terms of $x_A \in A_\beta$ (in particular, (6.14) holds also in this case), obtaining (6.15) with x_B replaced by $\tilde{x}$. The crucial difference is that the ratio in the r.h.s. of (6.15) is negative when $x_A \in A_\beta$; hence the proper sign must be introduced taking the square root of (6.15). This leads to $\tilde{x} = \text{Re}[z_{\text{inv}}(x_A)]$, where $z_{\text{inv}}(x_A)$ is given in (5.11) with $x_A \in A_\beta$. We remind that $\tilde{x}(x_A)$ is a bijective function from A_β onto $\mathbb{R}$.

In figure 9, considering only the positive half real axis without loss of generality, we display some geodesic bit threads that start at various $x_A \in A_\beta$, and therefore reach the horizon (grey dashed curves). Each geodesic bit thread of this kind is merged smoothly at the horizon with the corresponding geodesic (cyan dashed curves) that connects the horizon to the point $(\tilde{x}, 0)$ on the boundary, where $\tilde{x} = \text{Re}[z_{\text{inv}}(x_A)]$, as discussed above. The curves obtained from these geodesics are compared with the corresponding CFT curves described in section 5.2 (yellow solid curves, shown also in figure 5), that start at the same values of $x_A \in A_\beta$, grow in the strip $\{z \in \mathbb{C} \,; |\text{Im}(z)| \leqslant \beta/2\}$ according to (5.2) with $\theta \in (0, \pi)$ and end at $\text{Re}[z_{\text{inv}}(x_A)] + \mathrm{i}\frac{\beta}{2}$ when $\theta = \pi$. The relation $\tilde{x} = \text{Re}[z_{\text{inv}}(x_A)]$ is highlighted by the vertical dotted lines in figure 9.

7 Two disjoint intervals: massless Dirac field, ground state

In this section we consider the massless Dirac fermion in its ground state on the line bipartite by the union $A = A_1 \cup A_2$ of two disjoint intervals $A_1 = (a_1, b_1)$ and $A_2 = (a_2, b_2)$.

7.1 Internal modular evolution

The modular Hamiltonian of two disjoint intervals for a CFT in its ground state and on the line depends on the model. For the massless Dirac field, this modular Hamiltonian and the corresponding modular flow for the Dirac field have been described in [12, 13]. Casini and Huerta [12] found that this operator can be written as $K_A = K_A^{\text{loc}} + K_A^{\text{bi-loc}}$, where

$$K_A^{\text{loc}} = 2\pi \int_A \beta_{\text{loc}}(x) \, T_{tt}(t, x) \, \mathrm{d}x \tag{7.1}$$

is a local operator determined by the energy density $T_{tt}(t, x)$. For the massless Dirac field, the energy density reads[10]

$$T_{tt}(t, x) \equiv \frac{\mathrm{i}}{2} : \left[\left(\psi_1^* \left(\partial_x \psi_1 \right) - \left(\partial_x \psi_1^* \right) \psi_1 \right)(x + t) - \left(\psi_2^* \left(\partial_x \psi_2 \right) - \left(\partial_x \psi_2^* \right) \psi_2 \right)(x - t) \right] : \tag{7.2}$$

in terms of the chiral components ψ_1 and ψ_2 of the massless Dirac field. The bi-local term $K_A^{\text{bi-loc}}$ is

$$K_A^{\text{bi-loc}} = 2\pi \int_A \beta_{\text{bi-loc}}(x) \, T_{\text{bi-loc}}(t, x, x_c) \, \mathrm{d}x \tag{7.3}$$

---

[10]See the decomposition in eqs. (2.22)-(2.23) of [21].

where the bi-local operator $T_{\text{bi-loc}}(t, x, y)$ is the following quadratic operator

$$T_{\text{bi-loc}}(t, x, y) \equiv \frac{\mathrm{i}}{2} \left\{ : \!\! \left[\psi_1^*(x+t)\, \psi_1(y+t) - \psi_1^*(y+t)\, \psi_1(x+t) \right] \!\! : \right.$$
$$\left. + : \!\! \left[\psi_2^*(x-t)\, \psi_2(y-t) - \psi_2^*(y-t)\, \psi_2(x-t) \right] \!\! : \right\}. \qquad (7.4)$$

The weight functions in (7.1) and (7.3) can be written as

$$\beta_{\text{loc}}(x) = \frac{1}{w'(x)} \qquad \beta_{\text{bi-loc}}(x) = \frac{\beta_{\text{loc}}(x_{\text{c}}(x))}{x - x_{\text{c}}(x)} \qquad (7.5)$$

where

$$w(x) = \log\left[-\frac{(x - a_1)(x - a_2)}{(x - b_1)(x - b_2)}\right] \qquad (7.6)$$

which is the crucial function of our analysis throughout this section. This function naturally leads to introduce the point $x_{\text{c}}(x)$ conjugate to $x \in A$ through the condition $w(x_{\text{c}}(x)) = w(x)$. The explicit expression for $x_{\text{c}}(x)$ is [12, 20]

$$x_{\text{c}}(x) \equiv \frac{(b_1 b_2 - a_1 a_2)\, x + (b_1 + b_2)\, a_1 a_2 - (a_1 + a_2)\, b_1 b_2}{(b_1 - a_1 + b_2 - a_2)\, x + a_1 a_2 - b_1 b_2} = x_0 - \frac{R_0^2}{x - x_0} \qquad (7.7)$$

where

$$x_0 \equiv \frac{b_1 b_2 - a_1 a_2}{b_1 - a_1 + b_2 - a_2} \qquad R_0^2 \equiv \frac{(b_1 - a_1)(b_2 - a_2)(b_2 - a_1)(a_2 - b_1)}{(b_1 - a_1 + b_2 - a_2)^2}. \qquad (7.8)$$

Notice that a point x and its conjugate point $x_{\text{c}}(x)$ belong to different intervals in A. Furthermore, $x_{\text{c}}(x)$ in (7.7) is invariant under a cyclic permutation of the sequence of endpoints (a_1, b_1, a_2, b_2). It is sometimes convenient to write these expressions in terms of the lengths of the intervals $\ell_j \equiv b_j - a_j$ with $j \in \{1, 2\}$ and of the distance $d \equiv a_2 - b_1$ separating them. The conjugate point $x_{\text{c}}(x)$ in (7.7) should not be confused with the image of the geometric action of the modular conjugation. Indeed, for a given $x \in A$, while the former one still belongs to A, the latter one lies in the complement of A on the line.

The function providing the geometric action of the modular group of automorphisms induced by the vacuum reads [12, 13, 21]

$$\xi(\tau, x) \equiv \Theta_{A_1}(x)\, \xi_-(\tau, x) + \Theta_{A_2}(x)\, \xi_+(\tau, x) \qquad (7.9)$$

where $\Theta_{A_j}(x)$ is the characteristic function of A_j with $j \in \{1, 2\}$, and

$$\xi_\pm(\tau, x) \equiv w_\pm^{-1}\big(w(x) + 2\pi\tau\big) \qquad (7.10)$$

satisfying $\xi(0, x) = x$ for any $x \in A$. The functions in (7.10) are written in terms of the inverse functions $w_\pm^{-1}$ of (7.6), which are

$$w_\pm^{-1}(x) = \frac{a_1 + a_2 + (b_1 + b_2)\, e^x}{2(1 + e^x)} \pm \frac{\sqrt{\big(a_1 + a_2 + (b_1 + b_2)\, e^x\big)^2 - 4(1 + e^x)\,(a_1 a_2 + b_1 b_2\, e^x)}}{2(1 + e^x)}$$
$$(7.11)$$

where the expression under the square root is a quadratic polynomial in the variable e^x, whose discriminant is $-16(b_1 - a_1)(b_2 - a_2)(b_2 - a_1)(a_2 - b_1)$; hence it is positive for any $x \in \mathbb{R}$ when $a_1 < b_1 < a_2 < b_2$.

The map sending a generic configuration A of two intervals on the line into the symmetric configuration $A_{\text{sym}} \equiv (-b, -a) \cup (a, b)$, with $0 < a < b$, reads

$$f(x) \equiv \frac{a\big[a_1 a_2 - 2a_1 b_2 + a_2 b_2 + (a_1 - 2a_2 + b_2)\, x\big] + b\,(b_2 - a_1)(x - a_2)}{b\big[a_1 a_2 - 2a_1 b_2 + a_2 b_2 + (a_1 - 2a_2 + b_2)\, x\big] + a\,(b_2 - a_1)(x - a_2)}\, b \qquad (7.12)$$

where

$$\frac{b}{a} = \frac{a_1 b_1 + a_2 b_2 + b_1 b_2 + a_1 a_2 - 2(a_1 b_2 + a_2 b_1) + 2\sqrt{(b_1 - a_1)(b_2 - a_2)(a_2 - a_1)(b_2 - b_1)}}{(b_2 - a_1)(a_2 - b_1)}\,. \qquad (7.13)$$

Considering a point $x \in A$ and its conjugate $x_{\text{c}}(x) \in A$ given by (7.7), we observe that (7.12) satisfies

$$f(x)\, f(x_{\text{c}}(x)) = -a\,b\,. \qquad (7.14)$$

Let us introduce the points $c_j \in A_j$ with $j \in \{1, 2\}$ such that

$$f(x_{\text{c}}(c_j)) = -f(c_j)\,. \qquad (7.15)$$

Combining this definition with (7.14), one finds that $f(c_j)^2 = a\,b$ for these two points. From (7.15), their explicit expressions are

$$c_1 \equiv \frac{a_2 b_2 - a_1 b_1}{a_2 + b_2 - a_1 - b_1} - \frac{\sqrt{(a_2 - a_1)(a_2 - b_1)(b_2 - a_1)(b_2 - b_1)}}{a_2 + b_2 - a_1 - b_1} \qquad (7.16)$$

$$= a_1 + \frac{\sqrt{(\ell_1 + d)(\ell_1 + \ell_2 + d)}}{\ell_1 + \ell_2 + 2d}\left(\sqrt{(\ell_1 + d)(\ell_1 + \ell_2 + d)} - \sqrt{(\ell_2 + d)d}\right) \qquad (7.17)$$

and

$$c_2 \equiv \frac{a_2 b_2 - a_1 b_1}{a_2 + b_2 - a_1 - b_1} + \frac{\sqrt{(a_2 - a_1)(a_2 - b_1)(b_2 - a_1)(b_2 - b_1)}}{a_2 + b_2 - a_1 - b_1} \qquad (7.18)$$

$$= a_2 + \frac{\sqrt{(\ell_1 + d)\, d}}{\ell_1 + \ell_2 + 2d}\left(\sqrt{(\ell_2 + d)(\ell_1 + \ell_2 + d)} - \sqrt{(\ell_1 + d)d}\right). \qquad (7.19)$$

We also notice that $x_{\text{c}}(c_i) = c_j$ with $i \neq j$ and that

$$w(c_1) = w(c_2) = \log\left(\frac{a_2 - a_1}{b_2 - b_1}\right). \qquad (7.20)$$

In the case of the symmetric configuration A_{sym}, the function f in (7.12) is the identity map and the expression (7.7) for the conjugate point simplifies to $x_{\text{c}}(x) = -ab/x$, consistently with (7.14) for this configuration. In this case the condition (7.15) becomes $c_j^2 = ab$, which is the square of the geometric mean of a and b; hence $c_2 = \sqrt{ab} \in (a, b)$ and $c_1 = -\sqrt{ab} \in (-b, -a)$.

In the limit of large separation, i.e. when $d \to +\infty$, from (7.17) and (7.19) we have that $c_j = a_j + \ell_j/2 + O(1/d)$, with $j \in \{1, 2\}$. In the opposite limit of adjacent intervals, i.e.
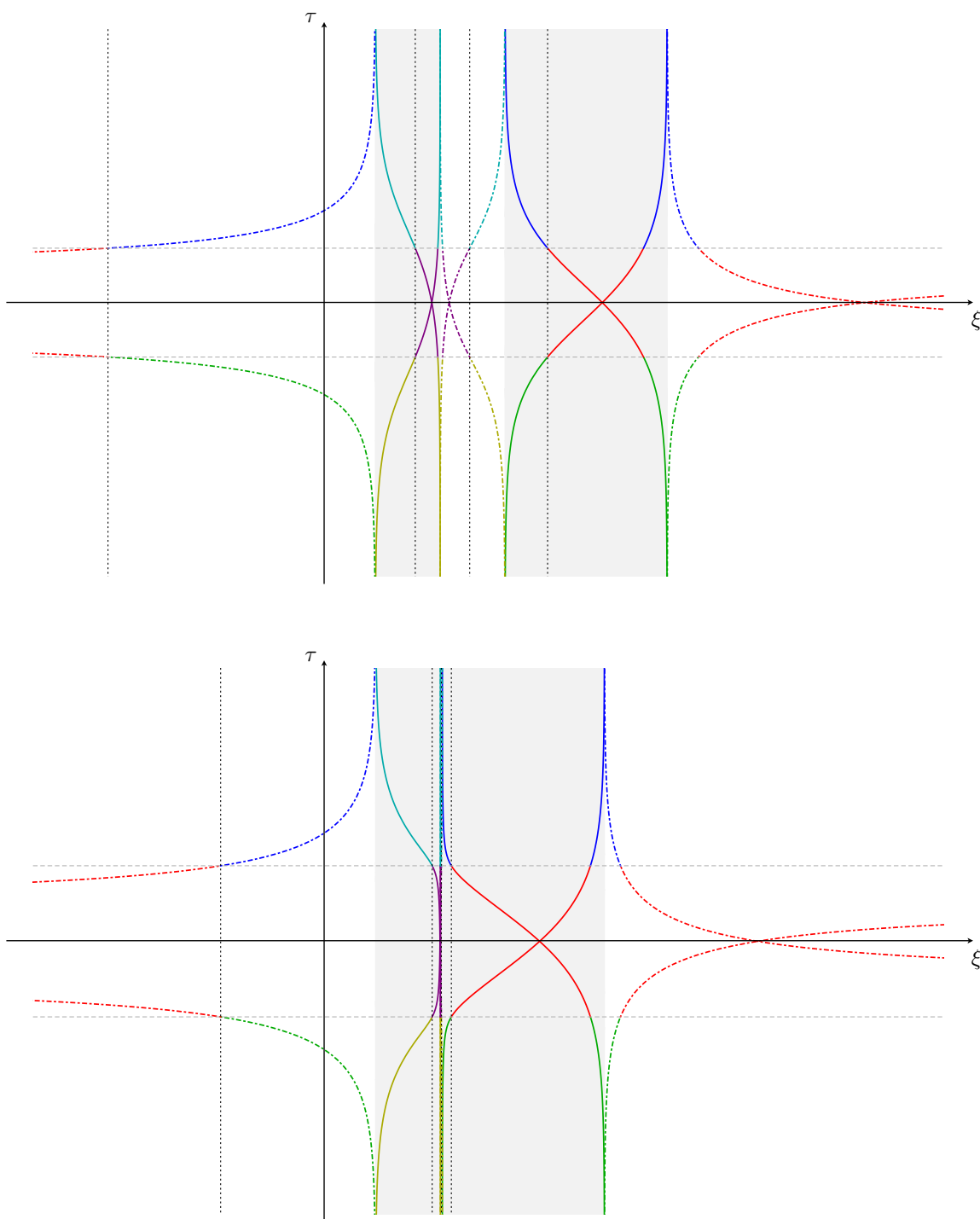
Figure 10. The curves $\xi(\tau, x)$ and $\xi(-\tau, x)$ (solid lines) and their images under the inversion map (dot-dashed lines) in the plane (ξ, τ), obtained from (7.9) and (7.26). The vertical dotted lines in the grey strips correspond to (7.16) and (7.18). The bottom panel illustrates the limiting regime of adjacent intervals.

when $d \to 0$ and the two intervals become the single interval (a_1, b_2), from (7.17) and (7.19) one finds that both c_1 and c_2 converge to the point $a_2 = b_1$ inside the final single interval.

In the top panel of figure 10 we consider the plane $\mathbb{R}^2$ parameterised by the coordinates (ξ, τ). The subsystem $A = A_1 \cup A_2$ provides the two grey vertical strips where $\xi \in A$, which contain the solid curves corresponding to $\xi(\tau, x)$ and $\xi(-\tau, x)$, obtained from (7.9) for a generic point $x \in A$ and its conjugate $x_c(x)$ at $\tau = 0$. The points (7.16) and (7.18) give the dotted vertical lines in these two grey strips. For any choice of $x \in A$ at $\tau = 0$, the intersection of these vertical lines with the solid curves is characterised by the condition $\xi(\tau_c, x) = c_j$ with $j \in \{1, 2\}$, which identifies the following value τ_c of the modular parameter

$$\tau_c(x) \equiv \frac{w(c_j) - w(x)}{2\pi} \qquad j \in \{1, 2\} \qquad (7.21)$$

where $w(c_j)$ is given by (7.20). From (7.20) and (7.21), we have that both c_1 and c_2 lead to the same value for $\tau_c(x)$ for any $x \in A$. This value naturally induces a partition of the solid curves obtained from (7.9) into three arcs corresponding to the partition $\mathbb{R} = (-\infty, -|\tau_c|) \cup (-|\tau_c|, |\tau_c|) \cup (|\tau_c|, +\infty)$ for the domain of τ, which are indicated through different colours in figure 10. The bottom panel of figure 10 displays the limit of adjacent intervals, identifying the arcs that remain non trivial and the ones that collapse either to vertical segments or to vertical half lines in this limit.

In the Minkowski spacetime parameterised by the coordinates (x, t), we have to consider the bipartition given by the union of two disjoint intervals A_1 and A_2 and its complement along each light ray direction (2.1). This leads to the spacetime domain $\mathcal{D}_A \equiv \mathcal{D}_1 \cup \mathcal{D}_2 \cup \mathcal{D}_{12}^+ \cup \mathcal{D}_{12}^-$, made by the union of the four grey regions shown in each the panels of figure 11: $\mathcal{D}_j$ are the diamonds corresponding to A_j, with $j \in \{1, 2\}$, and the two regions $\mathcal{D}_{12}^\pm$, which are symmetric with respect to the x-axis, are made by points of the spacetime where a light ray from A_1 and a light ray from A_2 intersect, travelling either in the future for $\mathcal{D}_{12}^+$ or in the past for $\mathcal{D}_{12}^-$.

A modular trajectory in $\mathcal{D}_A$ can be obtained by using (7.9) for each light ray coordinate. This leads to the following spacetime coordinates for the generic point of a modular trajectory

$$x(\tau) = \frac{\xi(\tau, p_{0,+}) + \xi(-\tau, p_{0,-})}{2} \qquad t(\tau) = \frac{\xi(\tau, p_{0,+}) - \xi(-\tau, p_{0,-})}{2} \qquad \tau \in \mathbb{R} \quad (7.22)$$

where $(u_+, u_-) = (p_{0,+}, p_{0,-})$ are the light ray coordinates of the initial point at $\tau = 0$.

Denote by $P = (u_{+,0}, u_{-,0})$ the light ray coordinates of the initial point of the modular evolution at $\tau = 0$, which must be both different from (7.16) and (7.18) to explore the most generic case. The light ray coordinates of the point P_c conjugate to P are $(x_c(u_{+,0}), x_c(u_{-,0}))$. In figure 11, two examples for P are shown: $P \in \mathcal{D}_2$ (black filled circle) and $P \in \mathcal{D}_{12}^+$ (blue filled circle). The corresponding P_c's are indicated with empty circles of the same colour. In order to obtain the expected modular trajectories for the single interval in the limit of adjacent intervals, beside the initial point P and its conjugate point P_c, we introduce also the two auxiliary points $P_{c,-} \equiv (u_{+,0}, x_c(u_{-,0}))$ and $P_{c,+} \equiv (x_c(u_{+,0}), u_{-,0})$, denoted by empty squares and empty rhombi in figure 11.
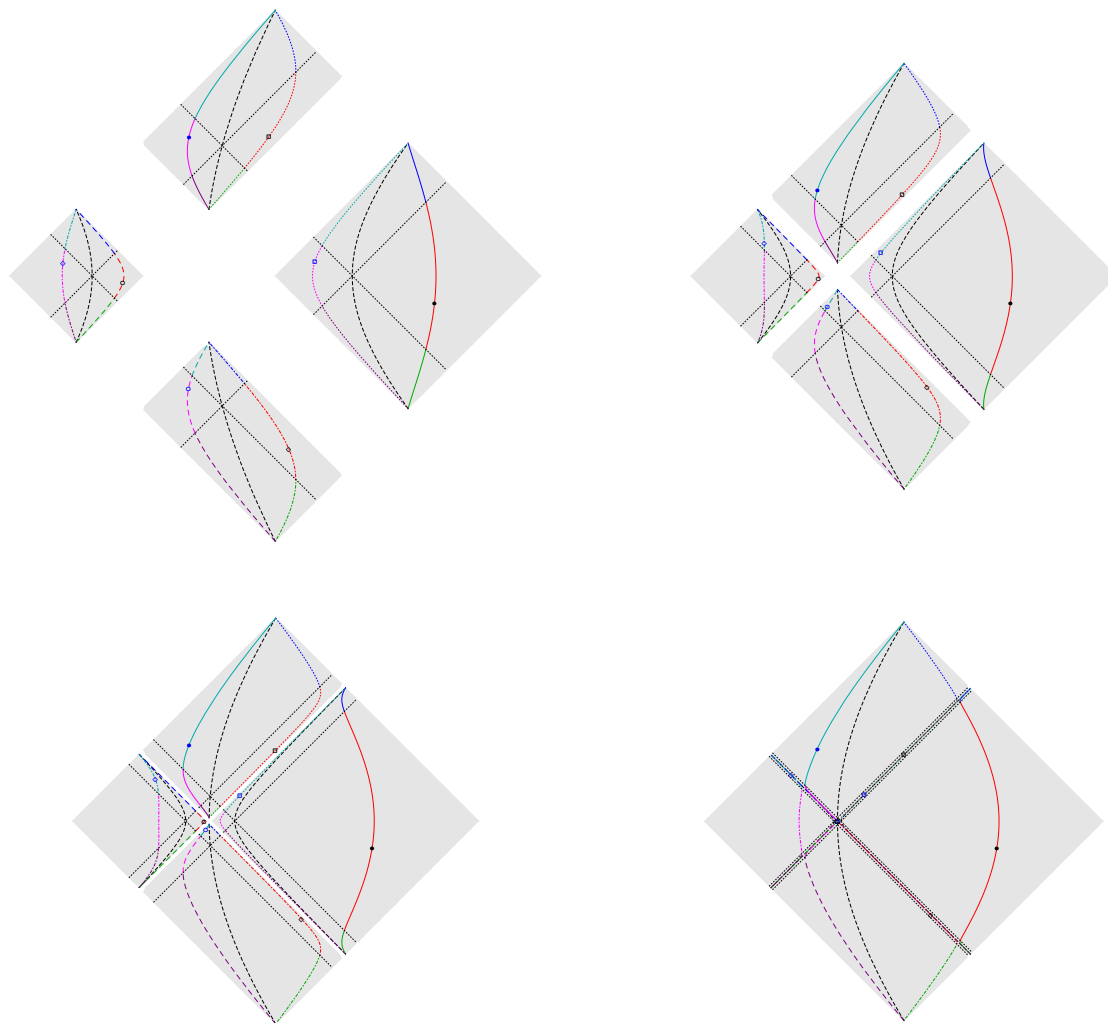
Figure 11. Spacetime domain $\mathcal{D}_A$ for the union of two disjoint intervals A_1 and A_2 on the line, whose lengths are $\ell_1 = \ell$ and $\ell_2 = 2\ell$ respectively. The distance d between the intervals changes in the different panels, while ℓ is kept fixed: $d/\ell = 1$ (top left), $d/\ell = 1/5$ (top right), $d/\ell = 1/20$ (bottom left) and $d/\ell = 1/1000$ (bottom right). The modular trajectories corresponding to following two choices of the initial point P are displayed: the black filled circle in $\mathcal{D}_2$ and the blue filled circle in $\mathcal{D}_{12}^+$. The empty symbols having the same colour denote the conjugate point P_c (empty circle) and the auxiliary points $P_{c,\pm}$ (empty square and empty rhombus) obtained from P.

The occurrence of the four points, which are the initial point P and its associated points P_c, $P_{c,+}$ and $P_{c,-}$, comes from the combination of the two different chiralities. Each region among $\mathcal{D}_1$, $\mathcal{D}_2$, $\mathcal{D}_{12}^+$ and $\mathcal{D}_{12}^-$ contains one and only one of these points. Choosing one of these four points at $\tau = 0$ and plugging its coordinates into (7.22), a modular trajectory is obtained in the corresponding region as $\tau \in \mathbb{R}$. Thus, we can associate four disjoint modular trajectories in $\mathcal{D}_A$ to any point $P \in \mathcal{D}_A$, which are in one-to-one correspondence with the four regions $\mathcal{D}_1$, $\mathcal{D}_2$, $\mathcal{D}_{12}^+$ and $\mathcal{D}_{12}^-$.

In figure 11 we show $\mathcal{D}_A$ for two disjoint intervals having assigned lengths, while the various panels correspond to different values of the distance separating them. The two

choices for P mentioned above are performed and each panel displays the four curves corresponding to each P. For a given P, the solid curve, the dashed curve, the dotted and the dot-dashed curves pass through P, $P_{\rm c}$ and $P_{{\rm c},\pm}$ respectively.

We find it instructive to consider also the four points C_1, C_2, C_{12}^+ and C_{12}^- whose light ray coordinates are obtained by combining (7.16) and (7.18) in all the four possible ways. These points correspond to the intersections of the black dotted segments in each panel of figure 11 and are in one-to-one correspondence with the regions $\mathcal{D}_1$, $\mathcal{D}_2$, $\mathcal{D}_{12}^+$ and $\mathcal{D}_{12}^-$; hence they are denoted in the same way. The null rays departing from each one of these four points (black dotted segments in figure 11) partition the corresponding grey region into four subregions. As a consequence, each one of the four points C_1, C_2, C_{12}^+ and C_{12}^- induces a natural partition of any modular trajectory belonging to the same region, which can be found by plugging its coordinates into (7.21) first and then partitioning the range $\mathbb{R}$ of the modular parameter accordingly. In figure 11, the components of the partition of each curve are indicated through different colours. The dashed black curves in figure 11 correspond to the modular trajectories passing through the points C_1, C_2, C_{12}^+ and C_{12}^-.

In figure 11, the sequence of panels shows the domain $\mathcal{D}_A$ of two disjoint intervals A_1 and A_2 with given lengths ℓ_1 and ℓ_2 for four decreasing values of the distance d separating them. This sequence illustrates how the four modular trajectories corresponding to a generic initial point P are deformed by the limiting procedure and finally provide the single modular trajectory in the final diamond of a single interval of length $\ell_1 + \ell_2$, obtained when A_1 and A_2 are adjacent and therefore share one endpoint. Various arcs of the different modular trajectories do not contribute to the final modular trajectory in the diamond of the adjacent intervals because they collapse to segments along null rays. In particular, taking $d \to 0$ in (7.16) and (7.18), one finds that all the points C_1, C_2, C_{12}^+ and C_{12}^- collapse to the shared endpoint. This implies that, considering the partition of each one of the four regions $\mathcal{D}_1$, $\mathcal{D}_2$, $\mathcal{D}_{12}^+$ and $\mathcal{D}_{12}^-$ identified by these points, only one component of the partition of each one of these four regions is non vanishing after the adjacent intervals limit. As for the four modular trajectories contained in $\mathcal{D}_A$, since each of them is partitioned accordingly to the partition induced by either C_1 or C_2 or C_{12}^+ or C_{12}^- of the region it belongs to, at most one component of their partition contributes to the final modular trajectory in the diamond of the adjacent intervals. The other arcs collapse on the light rays of the final shared endpoint, as shown in the bottom panels of figure 11. Notice that, beside the modular trajectory passing through the initial point P, only two other modular trajectories among the ones passing through $P_{\rm c}$ or $P_{{\rm c},\pm}$ contribute to the final modular trajectory after the limit $d \to 0$. It is instructive to compare the bottom right panel of figure 11 with the right panel of figure 1.

7.2 Geometric action in Euclidean spacetime

In order to explore the geometric action of the modular conjugation, we adapt to this case the analyses presented in section 3 and section 5. This leads us first to write an inversion map $z_{\rm inv}(x)$ on the real axis at $t = 0$ for $A = A_1 \cup A_2$ and its complement B on the line, and then to its extension to an inversion map on $\mathcal{D}_A$.

An inversion map for $A = A_1 \cup A_2$ and its complement B on the line can be constructed by exploiting the analysis in the Euclidean spacetime carried out in [17]. In the
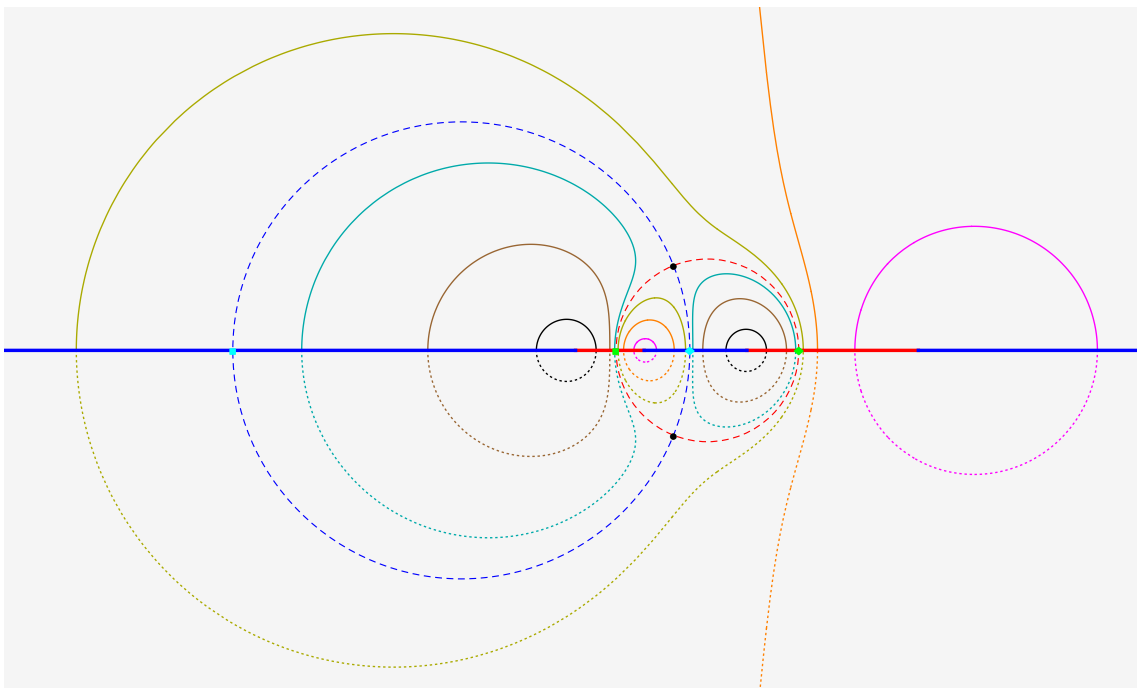
Figure 12. Euclidean modular evolution for the union $A = A_1 \cup A_2$ of two disjoint intervals (red segments), from (7.23) with either $\theta \in (0, \pi)$ (solid lines) or $\theta \in (\pi, 2\pi)$ (dotted lines), which lead to the inversion map (7.29) on the line. Curves having the same colour correspond to conjugate points in A.

complex plane parameterised by the complex variable z, the union of two disjoint intervals is identified through the endpoints of A_1 and A_2 (the entangling points) on the real axis. In figure 12, the subsystem A corresponds to the union of the two red segments and its complement B to the union of the blue ones; hence the four entangling points separate the red and blue segments, partitioning the real line. From the function $w(x)$ in (7.6) and its inverse functions (7.11), one constructs the following geometric action in the imaginary time [17]

$$z_{\pm}(\theta, x) \equiv w_{\pm}^{-1}(w(x) + \mathrm{i}\theta) \qquad \theta \in [0, 2\pi) \qquad x \in A \qquad (7.23)$$

which can be also obtained by replacing $2\pi\tau$ with $\mathrm{i}\theta$ in (7.10).

For any $x \in A$, the complex maps (7.23) allow to find a closed curve in the complex plane which intersects only once the real axis in B, when $\theta = \pi$ in (7.23). Similarly to the cases studied in section 3 and section 5, this observation provides a natural way to construct an inversion map $z_{\mathrm{inv},A}(x)$ sending A to its complement B on the real axis at $t = 0$. We require that a point close to an entangling point in A is mapped by this inversion to a point close to the same entangling point in B, and viceversa. In figure 12 we show the curves obtained from (7.23) for some $x \in A$ and for their conjugate points $x_{\mathrm{c}}(x)$ given by (7.7) (the curves with the same colour intersect A in x and $x_{\mathrm{c}}(x)$), as done in figure 9 of [17] for the special case of A_{sym}.

In order to write $z_{\mathrm{inv},A}(x)$, let us consider the points (7.16) and (7.18) (green points in figure 12). As observed in [17], these points can be found from the points in the complex

plane where $w'(z) = 0$, which are

$$z_{0,\pm} \equiv c_0 \pm \mathrm{i}\, \frac{\sqrt{(b_1 - a_1)(a_2 - b_1)(b_2 - a_1)(b_2 - a_2)}}{b_1 + b_2 - a_1 - a_2} \qquad c_0 \equiv \frac{b_1 b_2 - a_1 a_2}{b_1 + b_2 - a_1 - a_2} \,. \quad (7.24)$$

The points $z_{0,\pm}$ (black dots in figure 12) are the intersections of the circles C_a and C_b whose centers are on the real axis, in $(a_1 + a_2)/2$ and $(b_1 + b_2)/2$ respectively. In $z_{0,\pm}$, the straight lines tangent to C_a and C_b provide two supplementary angles whose bisectors allow to identify in a unique way two circles among the ones passing through $z_{0,\pm}$. One of these two circles (red dashed circle in figure 12) intersects the real axis at c_1 and c_2 given by (7.16) and (7.18) (green points), while the other one (blue dashed circle) intersects the real axis at d_1 and d_2 (cyan points in figure 12), obtained respectively from (7.16) and (7.18) modified through the cyclic shift of the ordered sequence of the endpoints $(a_1, b_1, a_2, b_2) \rightarrow (b_1, a_2, b_2, a_1)$.

In [17] it has been argued that the points (7.24) induce the occurrence of two critical values for $\theta \in (0, 2\pi)$ whose sum is 2π. One of these angles is $\theta_0 \equiv |\mathrm{Im}[w(z_{0,\pm})]|$; hence

$$\left| \tan \theta_0 \right| = \left| \frac{\mathrm{Im}\big[e^{w(z_{0,\pm})} \big]}{\mathrm{Re}\big[e^{w(z_{0,\pm})} \big]} \right| = \frac{2\sqrt{(b_1 - a_1)(b_2 - a_2)(a_2 - b_1)(b_2 - a_1)}}{\left| 2(a_1 a_2 + b_1 b_2) - (a_1 + a_2)(b_1 + b_2) \right|} \,. \quad (7.25)$$

From (7.23), (7.16) and (7.18) we construct the following inversion map on the line bipartite by the union of two disjoint intervals

$$
\begin{aligned}
z_{\mathrm{inv},A}(x) &\equiv
\begin{cases}
z_-(\pi, x) & x < c_1 \\
z_+(\pi, x) & x > c_1
\end{cases}
& x \in A_1 \\[2em]
z_{\mathrm{inv},A}(x) &\equiv
\begin{cases}
z_+(\pi, x) & x < c_2 \\
z_-(\pi, x) & x > c_2
\end{cases}
& x \in A_2
\end{aligned}
\qquad (7.26)
$$

which is one-to-one from A to B and maps points close to an entangling point into points close to the same entangling point.

At this stage let us introduce

$$\xi(\tau, x) \equiv \Theta_{B_1}(x)\, \xi_-(-\tau, x) + \Theta_{B_2}(x)\, \xi_+(-\tau, x) \qquad x \in B_1 \cup B_2 \qquad (7.27)$$

which has been employed to draw the dot-dashed curves in figure 10, obtained from (7.27) with x given by the image under (7.26) of the initial point in A providing the solid curves in the grey strips through (7.9).

In order to construct an inversion map $z_{\mathrm{inv}}(x)$ on the entire line, we have to describe also the one-to-one map inversion map $z_{\mathrm{inv},B}(x) : B \rightarrow A$ as the inverse of (7.26). This can be done by employing again the curves defined through (7.23), but now in the range $\theta \in (\pi, 2\pi)$. This leads to the curves in the lower half plane shown in figure 12 (dotted lines). Since the complement $B = B_1 \cup B_2 \in \mathbb{R}$ of A on the line is the union of $B_1 \equiv (b_1, a_2)$

and $B_2 \equiv (b_2, +\infty) \cup (-\infty, a_1)$, we find that $z_{\text{inv},B}(x)$ reads

$$z_{\text{inv},B}(x) \equiv \begin{cases} z_-(\pi, x) & x < d_1 \\ z_+(\pi, x) & x > d_1 \end{cases} \qquad x \in B_1$$

$$z_{\text{inv},B}(x) \equiv \begin{cases} z_-(\pi, x) & x < d_2 \\ z_+(\pi, x) & x > d_2 \end{cases} \qquad x \in B_2$$

(7.28)

where the points $d_j \in B_j$ with $j \in \{1, 2\}$ on the line introduced above (cyan points in figure 12).

Combining (7.26) and (7.28), we obtain the following inversion map on the line

$$z_{\text{inv}}(x) : \mathbb{R} \to \mathbb{R} \qquad\qquad z_{\text{inv}}(x) \equiv \begin{cases} z_{\text{inv},A}(x) & x \in A \\ z_{\text{inv},B}(x) & x \in B \end{cases} \qquad (7.29)$$

which is idempotent, as expected.

7.3 Geometric action in Minkowski spacetime

The idempotent map (7.29) allows to introduce the following inversion map for $\mathcal{D}_A$

$$x_{\text{inv}}(x, t) = \frac{z_{\text{inv}}(x + t) + z_{\text{inv}}(x - t)}{2} \qquad\qquad t_{\text{inv}}(x, t) = \frac{z_{\text{inv}}(x + t) - z_{\text{inv}}(x - t)}{2} \qquad (7.30)$$

which has the same structure of (3.5) and (5.21), explored in the previous analyses.

In figure 13, the map (7.30) sends $\mathcal{D}_A = \mathcal{D}_1 \cup \mathcal{D}_2 \cup \mathcal{D}_{12}^+ \cup \mathcal{D}_{12}^-$ (grey region, like in figure 11) into $\mathcal{W}_A$ (light blue region), and viceversa. Moreover, considering the vertices shared by $\mathcal{D}_A$ and $\mathcal{W}_A$, this map sends a point close to a vertex in the grey region into a point close to the same vertex in the blue region, and viceversa.

The four points labelled by black filled markers in $\mathcal{D}_A$ are obtained by combining (7.16) and (7.18) in all the four possible ways. Each one of these black points, which provides a natural partition of the rhombus it belongs to in four subregions (as already discussed in section 7.1 for figure 11) is mapped through the inversion (7.30) to the point in the light blue region labelled by the same marker coloured in red. Such red point induces a partition of the connected light blue region it belongs to in four subregions through the null rays departing from it. Anyone of the four subregions partitioning one of the four grey regions $\mathcal{D}_1$, $\mathcal{D}_2$, $\mathcal{D}_{12}^+$ and $\mathcal{D}_{12}^-$ is mapped by (7.30) into the subregion in the light blue domain that shares a vertex with it.

In figure 13 we display the modular trajectories corresponding to two initial points in $\mathcal{D}_A$ labelled by the blue and purple filled circles, as also done in figure 11 and by adopting the same conventions. In this figure we also show the images of these modular trajectories under the inversion map (7.30), that belong to $\mathcal{W}_A$. The images of the blue (purple) points are the green (yellow) points, labelled by the same kind of marker. The points labelled by empty markers are obtained from the one corresponding to the filled circle having the same colour, as discussed above for the points P_c and $P_{c,\pm}$ of figure 11. In figure 13 the image of each arc in $\mathcal{D}_A$ under (7.30) is the arc in $\mathcal{W}_A$ having the same colour and the same kind of
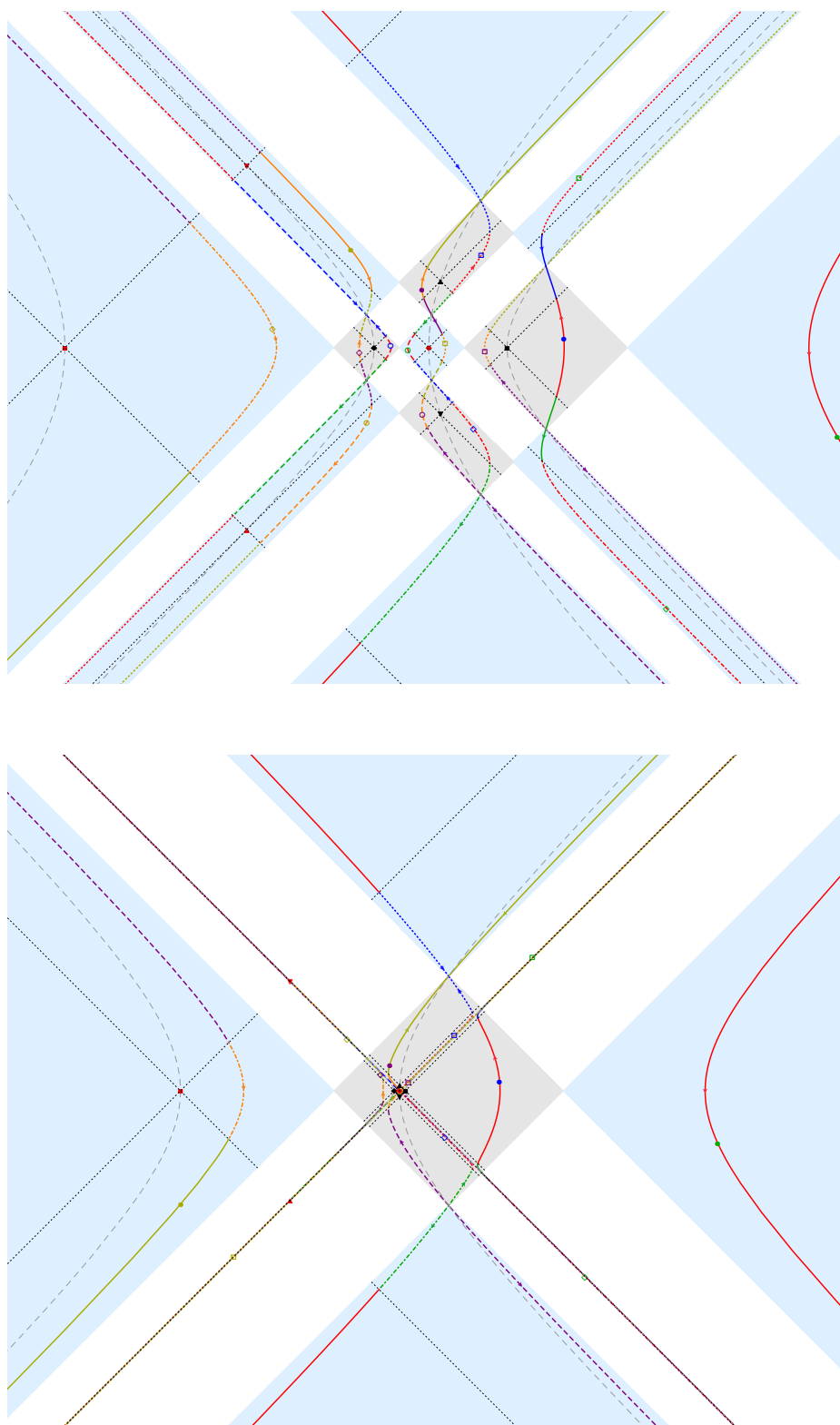
Figure 13. Modular trajectories in $\mathcal{D}_{A_1 \cup A_2}$ and their images under the inversion map (7.30). The bottom panel shows the limiting regime of adjacent intervals (see the right panel of figure 1).

line. The modular parameter τ grows along the curves as indicated by the arrows; hence the upper and lower vertices in $\mathcal{D}_1$, $\mathcal{D}_2$, $\mathcal{D}_{12}^+$ and $\mathcal{D}_{12}^-$ correspond to $\tau \to +\infty$ and $\tau \to -\infty$ respectively.

In figure 13 the black markers in $\mathcal{D}_A$ correspond to the four points C_1, C_2, C_{12}^+ and C_{12}^- introduced in section 7.1 and the red markers in $\mathcal{W}_A$ to their images under the inversion (7.30). The modular trajectories in $\mathcal{D}_A$ and their images under (7.30) in $\mathcal{W}_A$ are denoted by the grey dashed curves in the figure and we find it worth remarking that they do not display oscillations.

The bottom panel of figure 13 considers the curves displayed in the top panel of the same figure in the limit of adjacent intervals, showing that the right panel of figure 1 is recovered in this limiting regime.

We stress that the results described in this section hold for the massless Dirac field.

8   Conclusions

In this manuscript we have studied a holographic relation between the geometric action of some modular conjugations in 2D CFT and the geodesic bit threads considered in [35, 38] in a constant time slice of the corresponding dual gravitational backgrounds. This comparison has been performed for three cases and in all of them the bipartition of the space is given by a single interval: for a CFT in the ground state, either on the line (section 3 and section 4) or on the circle (appendices A and B), and in the thermal state on the line (section 5 and section 6).

When the CFT is in the ground state and on the line bipartite by an interval, the geometric actions of the modular operator and of the modular conjugation are described by the theorem of Hislop and Longo [2, 8, 9] and are given by (3.1) and (3.3) respectively. Considering for simplicity and without loss of generality the interval $A = (-b, b)$ on the line, the geometric action for the modular conjugation at $t = 0$ simplifies to (3.13). In the context of the gauge/gravity correspondence, this inversion relation is obtained between the endpoints of a geodesic bit thread on a constant time slice of Poincaré AdS$_3$ (see figure 3 and (4.9)). The case of a CFT in its ground state and on the circle bipartite by an interval is a straightforward generalisation whose geometric actions for the modular operator and the modular conjugation are (A.3) and (A.5) respectively. The corresponding holographic dual description of the geometric action of the modular conjugation is obtained through the geodesic bit threads in a constant time slice of global AdS$_3$ (see figure 15).

For a CFT in a thermal state at temperature $1/\beta$ and on the line bipartite by an interval, the geometric action of the modular conjugation is more insightful. In each chiral sector, the inversion map (5.5) on the bipartite line (see also (5.10)) obtained from the modular evolution in the Euclidean spacetime [17] naturally leads to introduce the subinterval $A_\beta \subset A$, whose endpoints are (5.6) and (5.7). Interestingly, denoting by ℓ the size of the interval A, we find that the integration over A_β of the corresponding contour function for the entanglement entropy [45] (see (5.16)) provides the Gibbs entropy $\pi\, c\, \ell/(3\beta)$ of an isolated system of length ℓ coming from the Stefan-Boltzmann law for a 2D CFT [43, 49, 50] for any value of ℓ and β. The inversion map (5.5) for a given chirality is a

complex function which acquires a constant non vanishing imaginary part on A_β and whose real part maps A_β into the second world (see figure 4). The occurrence of such spacetime is induced by the non triviality of the commutant for a thermal state, as discussed in [24–26, 28, 29]. The combination of the two different chiralities allows to extend this picture to the Minkowski spacetime $\mathcal{M}$ (see figure 6), where the geometric action of the modular conjugation is (5.23). Interestingly, this map is real also on the domain of dependence of A_β (green region in figure 6) and sends this diamond onto the entire Minkowski spacetime $\widetilde{\mathcal{M}}$ (which is interpreted as the second world) in a bijective way.

In the gauge/gravity correspondence, the restriction to the real line at $t = 0$ of this inversion map obtained for a 2D CFT in the (geometric) thermal state coincides with the relation between the endpoints of the geodesic bit threads on a constant time slice of the BTZ black brane geometry (see figure 8 and figure 9 for the geodesic bit threads anchored in $A \setminus A_\beta$ and in A_β respectively). The geodesic bit threads anchored in A_β reach the horizon.

It is instructive to compare the modular conjugation for the thermal case derived in section 5 with the thermo-field dynamic (TFD) setting of [52]. Both constructions are based on the Gibbs state generated by the Hamiltonian H of the system and adopt [53] the Tomita-Takesaki modular theory. In the TFD case one applies this theory to the whole system and the modular Hamiltonian is $H - JHJ$. Instead, in our case the modular Hamiltonian (5.24) is induced by the bipartition of the system in two parts A and B. For this reason the modular evolution and the modular conjugation in the two settings are different. Heuristically, our construction approaches the TFD setting when the interval A becomes the whole system. The TFD setup has been largely explored in AdS/CFT following [54], and, furthermore, the role of J in this context has been investigated in [55, 56].

Finally, for the massless Dirac fermion in the ground state and on the line bipartite by the union of two disjoint intervals, in section 7.2 we have proposed the inversion map (7.26), obtained by following [17] (see figure 12) and adapting the procedure established in the previous cases. This inversion map can be extended to the Minkowski spacetime through (7.30) (see figure 13). It is not difficult to realise that a holographic description of this inversion map on the real line cannot be found only through the geodesic bit threads in Poincaré AdS$_3$, as discussed in [38]. However, it could be insightful to find an explicit construction of holographic bit threads in Poincaré AdS$_3$ that reproduces the inversion map (7.26) holographically. We remark that, for a generic CFT in its ground state and the bipartition of the line given by the union of two disjoint intervals, a geometric action for the modular conjugation is not expected.

The analyses discussed in this manuscript can be extended in various directions. In $1 + 1$ spacetime dimensions, more complicated configurations can be investigated by considering e.g. a CFT at finite temperature and finite volume when the subsystem is still an interval [30–32, 57, 58] or a CFT in the ground state on the line when the bipartition is given by the union of an arbitrary number of disjoint intervals [12, 13, 59–61]. In higher dimensional CFT, it would be interesting to explore the action of the modular operators and of the modular conjugations for subregions having different shapes, comparing the results with the corresponding configurations of geodesic bit threads (see e.g. [62–68] for the shape dependence of the holographic entanglement entropy). Finally, we find it worth men-

tioning that various modular Hamiltonians in free models have been studied by taking the continuum limit of the corresponding operators (often called entanglement Hamiltonians) on the lattice [18, 69–80]. It would be insightful to study also other operators occurring in the Tomita-Takesaki modular theory in quantum many-body systems.

Acknowledgments

A Single interval on the circle: ground state

In this appendix we consider a CFT in its ground state and on a circle of length L bipartite by an interval $A = (a, b)$ and its complement. The circle can be represented by the interval $[-L/2 \, , L/2]$ whose endpoints $\pm L/2$ are identified.

In this case, the function $w(u)$ in the light ray coordinate u to employ in section 2 reads [16, 17]

$$w(u) = \log\left(\frac{\sin[\pi(u - a)/L]}{\sin[\pi(b - u)/L]}\right) \tag{A.1}$$

hence the weight function (2.4) for the entanglement Hamiltonian (2.3) is

$$\beta_0(u) \equiv \frac{L}{\pi} \, \frac{\sin[\pi(b - u)/L] \, \sin[\pi(u - a)/L]}{\sin[\pi(b - a)/L]} \, . \tag{A.2}$$

Specialising (2.9) to (A.1), one finds the geometric action of the modular automorphism group of the diamond induced by the ground state [21]

$$\xi(\tau, u) \, = \, \frac{L}{2\pi \, \mathrm{i}} \, \log\left(\frac{e^{\mathrm{i}\pi(b+a)/L} + e^{\mathrm{i}2\pi b/L} \, e^{w(u)+2\pi\tau}}{e^{\mathrm{i}\pi(b-a)/L} + e^{w(u)+2\pi\tau}}\right) \tag{A.3}$$

where $x \in A$ and $\tau \in \mathbb{R}$. In the Euclidean spacetime, the modular evolution (2.10) for this case becomes [17]

$$z(\theta, x) \, = \, \frac{L}{2\pi \, \mathrm{i}} \, \log\left(\frac{e^{\mathrm{i}\pi(b+a)/L} + e^{\mathrm{i}2\pi b/L} \, e^{w(x)+\mathrm{i}\theta}}{e^{\mathrm{i}\pi(b-a)/L} + e^{w(x)+\mathrm{i}\theta}}\right) \tag{A.4}$$

where $x \in A$ and $\theta \in [0, 2\pi)$. In the limit $L \to +\infty$, the expressions (A.3) and (A.4) become (3.1) and (3.16) respectively, as expected.

By adapting (3.22) and (5.5) (that hold for the CFT on the line at zero and finite temperature respectively) to this case, from (A.3) and (A.4) we introduce the inversion
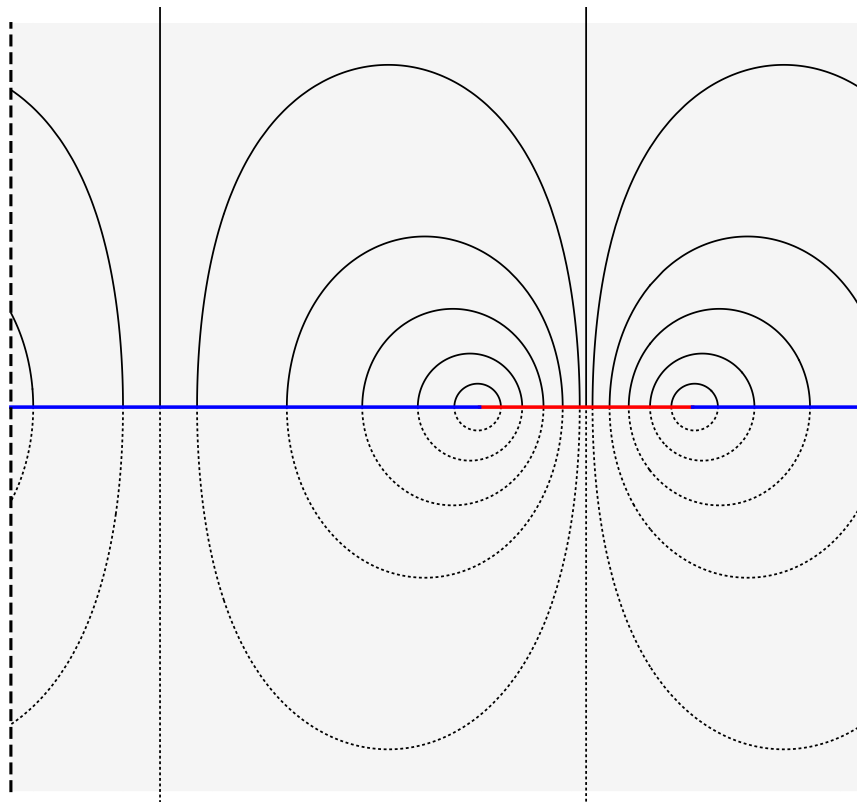
Figure 14. Euclidean modular evolution for a CFT in the ground state and on the circle bipartite by an interval (the dashed vertical line are identified). The curves are obtained from (A.4) for some $x \in A$, with either $\theta \in (0, \pi)$ (solid arcs) or $\theta \in (\pi, 2\pi)$ (dotted arcs). They map a point in A to a point in its complement on the circle (and viceversa), related by (A.5).

map for the CFT in the ground state and on the bipartite circle as follows

$$z_{\text{inv}}(x) \equiv \xi(\tau = \mathrm{i}/2 \, , x) = z(\theta = \pi \, , x) = \frac{L}{2\pi\,\mathrm{i}} \log\left(\frac{e^{\mathrm{i}\pi(b+a)/L} - e^{\mathrm{i}2\pi b/L}\, e^{w(x)}}{e^{\mathrm{i}\pi(b-a)/L} - e^{w(x)}}\right) \quad \text{(A.5)}$$

$$= b + \frac{L}{2\pi\,\mathrm{i}} \log\left(\frac{e^{w(x)} - e^{-\mathrm{i}\pi(b-a)/L}}{e^{w(x)} - e^{\mathrm{i}\pi(b-a)/L}}\right). \quad \text{(A.6)}$$

This function is real (see (A.6), where the argument of the logarithm is purely imaginary) and maps the interval A into its complement $B \equiv [-L/2 \, , L/2] \setminus A$.

In figure 14 the Euclidean spacetime $\{z \in \mathbb{C}; |\text{Re}(z)| \leqslant L/2\}$ is considered (grey region), where the two black vertical dashed lines at $|\text{Re}(z)| = L/2$ are identified. The red segment corresponds to the interval A and the blue segments to its complement B. The curves have been obtained from (A.4) for some $x \in A$, with either $\theta \in (0, \pi)$ (black solid curves) or $\theta \in (\pi, 2\pi)$ (black dotted curves). Their endpoints are related through the inversion map (A.5).

Let us discuss a consistency condition between the inversion map on the line (3.8) and the one (A.5) for the circle. The upper half plane in the complex coordinate μ and the

unit disk in the complex coordinate ν are related by the Cayley map

$$\nu(\mu) \,=\, -\frac{\mu - \mathrm{i}}{\mu + \mathrm{i}} \qquad\qquad \mu(\nu) \,=\, \mathrm{i}\,\frac{1 - \nu}{1 + \nu}\,. \tag{A.7}$$

This map relates also the boundaries of these two domains in the complex plane, i.e. the real line $\mathrm{Re}(\mu)$ and the unit circle $\{\nu = \mathrm{e}^{\mathrm{i}\theta}; \theta \in (-\pi, \pi]\}$ (notice that $\mu = 0$ is sent to $\theta = 0$ and $\mu \to \pm\infty$ to $\theta \to \pm\pi$). More precisely, a point $p \in \mathbb{R}$ is sent to $\mathrm{e}^{\mathrm{i}\theta_p}$ on the circle such that

$$\cos\theta_p = \frac{1 - p^2}{1 + p^2} \qquad\qquad \sin\theta_p = \frac{2\,p}{1 + p^2}\,. \tag{A.8}$$

Then, the map $\nu \to \frac{L}{2\pi\mathrm{i}}\log(\nu)$ can be used to send the unit circle onto the segment $[-L/2, L/2]$ whose endpoints are identified. Composing this transformation with the Cayley map, one finds a function that sends a point $p \in \mathbb{R}$ to a point $s \in [-L/2, L/2]$ in the above segment as follows

$$s(p) = \frac{L}{2\pi\mathrm{i}}\log[\nu(p)] = \frac{L\,\theta_p}{2\pi}\,. \tag{A.9}$$

Considering the inversion map $z_{\mathrm{inv}}(x)$ on the line (see (3.4) and (3.8)) for $x \in (a, b) \subset \mathbb{R}$ and denoting (A.5) by $\tilde{z}_{\mathrm{inv}}(L, a, b; x)$ to avoid confusion, one finds that

$$s\big(z_{\mathrm{inv}}(x)\big) \,=\, \tilde{z}_{\mathrm{inv}}\big(L, s(a), s(b); s(x)\big) \tag{A.10}$$

which tells us that the inversion maps at $t = 0$ discussed in section 3.2 and in this appendix can be related through conformal mappings.

B Geodesic bit threads in global AdS$_3$

In this appendix we show that the inversion map discussed in the appendix A can be obtained also through the geodesic bit threads in a constant time slice of global AdS$_3$.

The metric on a fixed time slice of AdS$_3$ in global coordinates reads

$$ds^2 \,=\, d\rho^2 + (\sinh\rho)^2 d\theta^2 \,=\, \frac{4}{(1 - r^2)^2}\,\big(dr^2 + r^2 d\theta^2\big) \qquad\qquad \rho = \log\!\left(\frac{1 + r}{1 - r}\right) \tag{B.1}$$

where $\rho \geqslant 0$ and $\theta \in [0, 2\pi)$. The last expression in (B.1) is written in terms of the polar coordinates (r, θ), with $0 \leqslant r < 1$, and corresponds to the Poincaré disk (yellow unit disk in figure 15). The Cayley map (A.7) relates the upper half plane, in the complex coordinate $\mu = x + \mathrm{i}\zeta$ and equipped with the hyperbolic metric (4.1), to the Poincaré disk with the metric (B.1) in the complex coordinate $\nu = r\,\mathrm{e}^{\mathrm{i}\theta}$.

The geodesics in the Poincaré disk having their endpoints on the boundary are circular arcs that intersect the boundary orthogonally. In a disk of radius R in polar coordinates (r, θ), where $0 \leqslant r \leqslant R$, the orthogonality condition for the intersection of two circles provides the following second order equation

$$\big(r^2 + R^2\big)\cos\alpha - 2\,r\,R\cos(\theta - \theta_0) = 0 \tag{B.2}$$
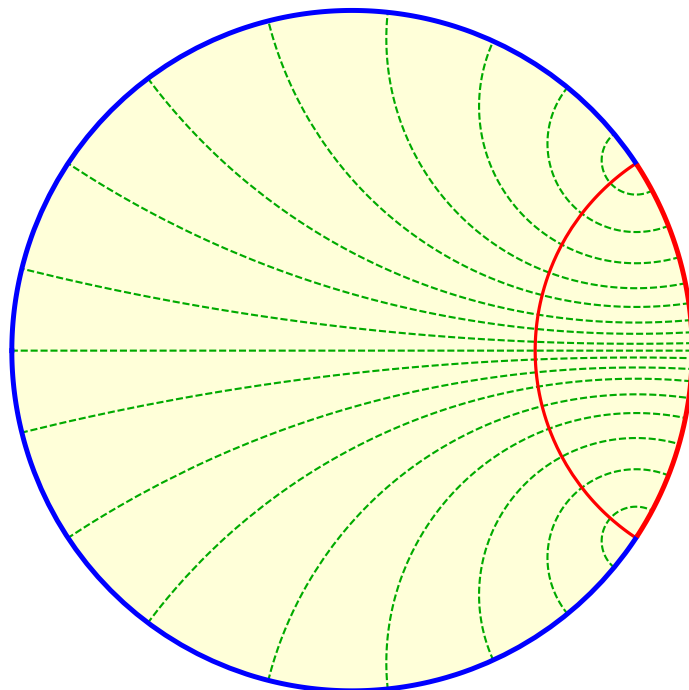
Figure 15. Geodesic bit threads (green dashed circular arcs) in a fixed time slice of global AdS₃ (yellow unit disk, see (B.1)) for an arc of the boundary circle (red arc), whose RT curve is the red solid arc anchored to its endpoints.

where the intersections occur at (R, θ_+) and (R, θ_-) in polar coordinates, with $\theta_\pm \equiv \theta_0 \pm \alpha$. Solving (B.2), for the arc inside the disk one finds

$$ r \,=\, R \, \frac{\cos(\theta - \theta_0) - \sqrt{[\cos(\theta - \theta_0)]^2 - (\cos\alpha)^2}}{\cos\alpha} \qquad\qquad \theta \in (\theta_- , \theta_+) \qquad \text{(B.3)} $$

where $R = 1$ for the Poincaré disk.

Consider the interval $(-b, b) \subset \mathbb{R}$, as done in section 4. The corresponding arc on the boundary of the Poincaré disk (red arc on the boundary of the unit disk in figure 15) is given by $|\theta| \leqslant \alpha_{\mathrm{RT}}$, where $\cos\alpha_{\mathrm{RT}} = (1 - b^2)/(1 + b^2) = \mathrm{Re}[\nu(b)]$, from (A.8). Hence the RT curve in the Poincaré disk is given by (B.3) specialised to $R = 1$, $\theta_0 = 0$ and $\alpha = \alpha_{\mathrm{RT}}$. In figure 15, it corresponds to the red curve in the bulk of the Poincaré disk.

The geodesic bit threads in the Poincaré disk for this RT curve can be also found through the Cayley map. The angular coordinates $\theta_\pm$ of the endpoints are obtained from (A.8) with $p = x_s \pm R_s$. These coordinates give the parameters α an θ_0 (in terms of $x_A \in (-b, b)$) to employ in (B.3) with $R = 1$ in order to find the geodesic bit threads. Some of them are shown in figure 15 (green dashed circular arcs).

Finally, by employing also the map $\nu \to \frac{L}{2\pi i} \log(\nu)$ introduced in the appendix A, we have checked that the angular distance between the endpoints of a geodesic bit thread agrees with the CFT expression (A.5), as expected.

References

[1] M. Takesaki, *Tomita's theory of modular Hilbert algebras and its applications*, Springer (1970).

[2] R. Haag, *Local quantum physics: fields, particles, algebras*, Springer (1996).

[3] O. Bratteli and D.W. Robinson, *Operator algebras and quantum statistical mechanics II: Equilibrium states. Models in quantum statistical mechanics*, Springer (1996).

[4] H.J. Borchers, *On revolutionizing quantum field theory with Tomita's modular theory*, *J. Math. Phys.* **41** (2000) 3604 [INSPIRE].

[5] M. Takesaki, *Theory of operator algebras II*, Springer (2003).

[6] J.J. Bisognano and E.H. Wichmann, *On the duality condition for a Hermitian scalar field*, *J. Math. Phys.* **16** (1975) 985 [INSPIRE].

[7] J.J. Bisognano and E.H. Wichmann, *On the duality condition for quantum fields*, *J. Math. Phys.* **17** (1976) 303 [INSPIRE].

[8] P.D. Hislop and R. Longo, *Modular structure of the local algebras associated with the free massless scalar field theory*, *Commun. Math. Phys.* **84** (1982) 71 [INSPIRE].

[9] R. Brunetti, D. Guido and R. Longo, *Modular structure and duality in conformal quantum field theory*, *Commun. Math. Phys.* **156** (1993) 201 [funct-an/9302008] [INSPIRE].

[10] T. Saffary, *On the generator of massive modular groups*, *Lett. Math. Phys.* **77** (2006) 235 [math-ph/0601036] [INSPIRE].

[11] T. Saffary, *Modular action on the massive algebra*, Ph.D. thesis, Hamburg U., Hamburg, Germany (2005) [math-ph/0512046] [INSPIRE].

[12] H. Casini and M. Huerta, *Reduced density matrix and internal dynamics for multicomponent regions*, *Class. Quant. Grav.* **26** (2009) 185005 [arXiv:0903.5284] [INSPIRE].

[13] R. Longo, P. Martinetti and K.-H. Rehren, *Geometric modular action for disjoint intervals and boundary conformal field theory*, *Rev. Math. Phys.* **22** (2010) 331 [arXiv:0912.1106] [INSPIRE].

[14] K.-H. Rehren and G. Tedesco, *Multilocal fermionization*, *Lett. Math. Phys.* **103** (2013) 19 [arXiv:1205.0324] [INSPIRE].

[15] H. Casini, M. Huerta and R.C. Myers, *Towards a derivation of holographic entanglement entropy*, *JHEP* **05** (2011) 036 [arXiv:1102.0440] [INSPIRE].

[16] G. Wong, I. Klich, L.A. Pando Zayas and D. Vaman, *Entanglement temperature and entanglement entropy of excited states*, *JHEP* **12** (2013) 020 [arXiv:1305.3291] [INSPIRE].

[17] J. Cardy and E. Tonni, *Entanglement hamiltonians in two-dimensional conformal field theory*, *J. Stat. Mech.* **1612** (2016) 123103 [arXiv:1608.01283] [INSPIRE].

[18] R. Arias, D. Blanco, H. Casini and M. Huerta, *Local temperatures and local terms in modular Hamiltonians*, *Phys. Rev. D* **95** (2017) 065005 [arXiv:1611.08517] [INSPIRE].

[19] E. Tonni, J. Rodríguez-Laguna and G. Sierra, *Entanglement Hamiltonian and entanglement contour in inhomogeneous 1D critical systems*, *J. Stat. Mech.* **1804** (2018) 043105 [arXiv:1712.03557] [INSPIRE].

[20] R.E. Arias, H. Casini, M. Huerta and D. Pontello, *Entropy and modular Hamiltonian for a free chiral scalar in two intervals*, *Phys. Rev. D* **98** (2018) 125008 [arXiv:1809.00026] [INSPIRE].

[21] M. Mintchev and E. Tonni, *Modular Hamiltonians for the massless Dirac field in the presence of a boundary*, *JHEP* **03** (2021) 204 [arXiv:2012.00703] [INSPIRE].

[22] M. Mintchev and E. Tonni, *Modular Hamiltonians for the massless Dirac field in the presence of a defect*, *JHEP* **03** (2021) 205 [arXiv:2012.01366] [INSPIRE].

[23] H.J. Borchers and J. Yngvason, *Modular groups of quantum fields in thermal states*, *J. Math. Phys.* **40** (1999) 601 [math-ph/9805013] [INSPIRE].

[24] H.J. Borchers, *On thermal states in* $(1+1)$*-dimensional quantum systems*, unpublished (1998).

[25] B. Schroer and H.W. Wiesbrock, *Looking beyond the thermal horizon: hidden symmetries in chiral models*, *Rev. Math. Phys.* **12** (2000) 461 [hep-th/9901031] [INSPIRE].

[26] R. Longo, *Notes for a quantum index theorem*, *Commun. Math. Phys.* **222** (2001) 45 [math.OA/0003082] [INSPIRE].

[27] D. Buchholz, C. D'Antoni and R. Longo, *Nuclearity and thermal states in conformal field theory*, *Commun. Math. Phys.* **270** (2007) 267 [math-ph/0603083] [INSPIRE].

[28] P. Camassa, R. Longo, Y. Tanimoto and M. Weiner, *Thermal states in conformal QFT. I*, *Commun. Math. Phys.* **309** (2012) 5 [arXiv:1101.2865] [INSPIRE].

[29] P. Camassa, R. Longo, Y. Tanimoto and M. Weiner, *Thermal states in conformal QFT. II*, *Commun. Math. Phys.* **315** (2012) 771 [arXiv:1109.2064] [INSPIRE].

[30] S. Hollands, *On the modular operator of multi-component regions in chiral CFT*, *Commun. Math. Phys.* **384** (2021) 785 [arXiv:1904.08201] [INSPIRE].

[31] D. Blanco and G. Pérez-Nadal, *Modular Hamiltonian of a chiral fermion on the torus*, *Phys. Rev. D* **100** (2019) 025003 [arXiv:1905.05210] [INSPIRE].

[32] P. Fries and I.A. Reyes, *Entanglement spectrum of chiral fermions on the torus*, *Phys. Rev. Lett.* **123** (2019) 211603 [arXiv:1905.05768] [INSPIRE].

[33] S. Ryu and T. Takayanagi, *Holographic derivation of entanglement entropy from AdS/CFT*, *Phys. Rev. Lett.* **96** (2006) 181602 [hep-th/0603001] [INSPIRE].

[34] S. Ryu and T. Takayanagi, *Aspects of holographic entanglement entropy*, *JHEP* **08** (2006) 045 [hep-th/0605073] [INSPIRE].

[35] M. Freedman and M. Headrick, *Bit threads and holographic entanglement*, *Commun. Math. Phys.* **352** (2017) 407 [arXiv:1604.00354] [INSPIRE].

[36] M. Headrick and V.E. Hubeny, *Riemannian and Lorentzian flow-cut theorems*, *Class. Quant. Grav.* **35** (2018) 10 [arXiv:1710.09516] [INSPIRE].

[37] V.E. Hubeny, *Bulk locality and cooperative flows*, *JHEP* **12** (2018) 068 [arXiv:1808.05313] [INSPIRE].

[38] C.A. Agón, J. De Boer and J.F. Pedraza, *Geometric aspects of holographic bit threads*, *JHEP* **05** (2019) 075 [arXiv:1811.08879] [INSPIRE].

[39] M. Headrick, J. Held and J. Herman, *Crossing versus locking: bit threads and continuum multiflows*, *Commun. Math. Phys.* **396** (2022) 265 [arXiv:2008.03197] [INSPIRE].

[40] J. Harper and M. Headrick, *Bit threads and holographic entanglement of purification*, *JHEP* **08** (2019) 101 [arXiv:1906.05970] [INSPIRE].

[41] M. Headrick and V.E. Hubeny, *Covariant bit threads*, arXiv:2208.10507 [INSPIRE].

[42] M. Luscher, *How to derive the Virasoro algebra from dilation invariance*, unpublished notes (1988).

[43] J. Cardy, *The ubiquitous 'c': from the Stefan-Boltzmann law to quantum information*, *J. Stat. Mech.* **1010** (2010) P10004 [arXiv:1008.2331] [INSPIRE].

[44] Y. Chen and G. Vidal, *Entanglement contour*, *J. Stat. Mech.* **2014** (2014) P10011 [arXiv:1406.1471].

[45] A. Coser, C. De Nobili and E. Tonni, *A contour for the entanglement entropies in harmonic lattices*, *J. Phys. A* **50** (2017) 314001 [arXiv:1701.08427] [INSPIRE].

[46] E. Tonni, *Entanglement Hamiltonians and contours in a segment*, talk delivered at the *It from Qubit workshop*, https://www.youtube.com/watch?v=nO0gL4TZfy8, Centro Atómico Bariloche, San Carlos de Bariloche, Argentina, January 2018.

[47] J. Kudler-Flam, I. MacCormack and S. Ryu, *Holographic entanglement contour, bit threads, and the entanglement tsunami*, *J. Phys. A* **52** (2019) 325401 [arXiv:1902.04654] [INSPIRE].

[48] P. Calabrese and J.L. Cardy, *Entanglement entropy and quantum field theory*, *J. Stat. Mech.* **0406** (2004) P06002 [hep-th/0405152] [INSPIRE].

[49] H.W.J. Bloete, J.L. Cardy and M.P. Nightingale, *Conformal invariance, the central charge, and universal finite size amplitudes at criticality*, *Phys. Rev. Lett.* **56** (1986) 742 [INSPIRE].

[50] I. Affleck, *Universal term in the free energy at a critical point and the conformal anomaly*, *Phys. Rev. Lett.* **56** (1986) 746 [INSPIRE].

[51] G. Di Giulio, R. Arias and E. Tonni, *Entanglement Hamiltonians in 1D free lattice models after a global quantum quench*, *J. Stat. Mech.* **1912** (2019) 123103 [arXiv:1905.01144] [INSPIRE].

[52] Y. Takahashi and H. Umezawa, *Thermo field dynamics*, *Int. J. Mod. Phys. B* **10** (1996) 1755 [INSPIRE].

[53] I. Ojima, *Gauge fields at finite temperatures: thermo field dynamics, KMS condition and their extension to gauge theories*, *Annals Phys.* **137** (1981) 1 [INSPIRE].

[54] J.M. Maldacena, *Eternal black holes in anti-de Sitter*, *JHEP* **04** (2003) 021 [hep-th/0106112] [INSPIRE].

[55] K. Papadodimas and S. Raju, *An infalling observer in AdS/CFT*, *JHEP* **10** (2013) 212 [arXiv:1211.6767] [INSPIRE].

[56] K. Papadodimas and S. Raju, *State-dependent bulk-boundary maps and black hole complementarity*, *Phys. Rev. D* **89** (2014) 086010 [arXiv:1310.6335] [INSPIRE].

[57] M. Headrick and T. Takayanagi, *A holographic proof of the strong subadditivity of entanglement entropy*, *Phys. Rev. D* **76** (2007) 106013 [arXiv:0704.3719] [INSPIRE].

[58] V.E. Hubeny, H. Maxfield, M. Rangamani and E. Tonni, *Holographic entanglement plateaux*, *JHEP* **08** (2013) 092 [arXiv:1306.4004] [INSPIRE].

[59] M. Headrick, *Entanglement Rényi entropies in holographic theories*, *Phys. Rev. D* **82** (2010) 126010 [arXiv:1006.0047] [INSPIRE].

[60] E. Tonni, *Holographic entanglement entropy: near horizon geometry and disconnected regions*, *JHEP* **05** (2011) 004 [arXiv:1011.0166] [INSPIRE].

[61] A. Coser, L. Tagliacozzo and E. Tonni, *On Rényi entropies of disjoint intervals in conformal field theory*, *J. Stat. Mech.* **1401** (2014) P01008 [arXiv:1309.2189] [INSPIRE].

[62] I.R. Klebanov, T. Nishioka, S.S. Pufu and B.R. Safdi, *On shape dependence and RG flow of entanglement entropy*, *JHEP* **07** (2012) 001 [arXiv:1204.4160] [INSPIRE].

[63] A. Allais and M. Mezei, *Some results on the shape dependence of entanglement and Rényi entropies*, *Phys. Rev. D* **91** (2015) 046002 [arXiv:1407.7249] [INSPIRE].

[64] P. Fonda, L. Giomi, A. Salvio and E. Tonni, *On shape dependence of holographic mutual information in AdS$_4$*, *JHEP* **02** (2015) 005 [arXiv:1411.3608] [INSPIRE].

[65] P. Fonda, D. Seminara and E. Tonni, *On shape dependence of holographic entanglement entropy in AdS$_4$/CFT$_3$*, *JHEP* **12** (2015) 037 [arXiv:1510.03664] [INSPIRE].

[66] D. Seminara, J. Sisti and E. Tonni, *Holographic entanglement entropy in AdS$_4$/BCFT$_3$ and the Willmore functional*, *JHEP* **08** (2018) 164 [arXiv:1805.11551] [INSPIRE].

[67] G. Cavini, D. Seminara, J. Sisti and E. Tonni, *On shape dependence of holographic entanglement entropy in AdS$_4$/CFT$_3$ with Lifshitz scaling and hyperscaling violation*, *JHEP* **02** (2020) 172 [arXiv:1907.10030] [INSPIRE].

[68] P. Bueno, H. Casini, O.L. Andino and J. Moreno, *Disks globally maximize the entanglement entropy in $2+1$ dimensions*, *JHEP* **10** (2021) 179 [arXiv:2107.12394] [INSPIRE].

[69] I. Peschel, *Calculation of reduced density matrices from correlation functions*, *J. Phys. A* **36** (2003) L205 [cond-mat/0212631].

[70] H. Casini and M. Huerta, *Entanglement entropy in free quantum field theory*, *J. Phys. A* **42** (2009) 504007 [arXiv:0905.2562] [INSPIRE].

[71] I. Peschel and V. Eisler, *Reduced density matrices and entanglement entropy in free lattice models*, *J. Phys. A* **42** (2009) 504003 [arXiv:0906.1663].

[72] L. Banchi, S.L. Braunstein and S. Pirandola, *Quantum fidelity for arbitrary Gaussian states*, *Phys. Rev. Lett.* **115** (2015) 260501 [arXiv:1507.01941].

[73] V. Eisler and I. Peschel, *Analytical results for the entanglement Hamiltonian of a free-fermion chain*, *J. Phys. A* **50** (2017) 284003 [arXiv:1703.08126] [INSPIRE].

[74] V. Eisler and I. Peschel, *Properties of the entanglement Hamiltonian for finite free-fermion chains*, *J. Stat. Mech.* **1810** (2018) 104001 [arXiv:1805.00078] [INSPIRE].

[75] V. Eisler, E. Tonni and I. Peschel, *On the continuum limit of the entanglement Hamiltonian*, *J. Stat. Mech.* **1907** (2019) 073101 [arXiv:1902.04474] [INSPIRE].

[76] G. Di Giulio and E. Tonni, *On entanglement Hamiltonians of an interval in massless harmonic chains*, *J. Stat. Mech.* **2003** (2020) 033102 [arXiv:1911.07188] [INSPIRE].

[77] N. Javerzat and E. Tonni, *On the continuum limit of the entanglement Hamiltonian of a sphere for the free massless scalar field*, *JHEP* **02** (2022) 086 [arXiv:2111.05154] [INSPIRE].

[78] V. Eisler, G. Di Giulio, E. Tonni and I. Peschel, *Entanglement Hamiltonians for non-critical quantum chains*, *J. Stat. Mech.* **2010** (2020) 103102 [arXiv:2007.01804] [INSPIRE].

[79] F. Rottoli, S. Scopa and P. Calabrese, *Entanglement Hamiltonian during a domain wall melting in the free Fermi chain*, *J. Stat. Mech.* **2206** (2022) 063103 [arXiv:2202.04380] [INSPIRE].

[80] V. Eisler, E. Tonni and I. Peschel, *Local and non-local properties of the entanglement Hamiltonian for two disjoint intervals*, *J. Stat. Mech.* **2208** (2022) 083101 [arXiv:2204.03966] [INSPIRE].